



Lawrence Berkeley Laboratory

UNIVERSITY OF CALIFORNIA

RECEIVED
LAWRENCE
BERKELEY LABORATORY
AUG 12 1986

EARTH SCIENCES DIVISION

LIBRARY AND
DOCUMENTS SECTION

Submitted to Journal of Geophysical Research

THERMOHYDROLOGICAL CONDITIONS AND SILICA
REDISTRIBUTION NEAR HIGH-LEVEL NUCLEAR WASTES
EMPLACED IN SATURATED GEOLOGICAL FORMATIONS

A. Verma and K. Pruess

May 1986

TWO-WEEK LOAN COPY

*This is a Library Circulating Copy
which may be borrowed for two weeks.*



LBL-21613
c. 2

DISCLAIMER

This document was prepared as an account of work sponsored by the United States Government. While this document is believed to contain correct information, neither the United States Government nor any agency thereof, nor the Regents of the University of California, nor any of their employees, makes any warranty, express or implied, or assumes any legal responsibility for the accuracy, completeness, or usefulness of any information, apparatus, product, or process disclosed, or represents that its use would not infringe privately owned rights. Reference herein to any specific commercial product, process, or service by its trade name, trademark, manufacturer, or otherwise, does not necessarily constitute or imply its endorsement, recommendation, or favoring by the United States Government or any agency thereof, or the Regents of the University of California. The views and opinions of authors expressed herein do not necessarily state or reflect those of the United States Government or any agency thereof or the Regents of the University of California.

**THERMOHYDROLOGICAL CONDITIONS AND SILICA
REDISTRIBUTION NEAR HIGH-LEVEL NUCLEAR WASTES
EMPLACED IN SATURATED GEOLOGICAL FORMATIONS**

A. Verma and K. Pruess

Earth Sciences Division
Lawrence Berkeley Laboratory
University of California
Berkeley, California 94720

May 1986

Prepared for

Waste Management Branch
Division of Radiation Programs and Earth Sciences
Office of Nuclear Regulatory Research
U.S. Nuclear Regulatory Commission
Washington, D.C. 20555

This work was supported by the U.S. Nuclear Regulatory Commission, through NRC Fin No. B3046-3 under Interagency Agreements DOE-60-83-388 and 60-83-367, through U.S. Department of Energy Contract No. DE-AC03-76SF00098.

ABSTRACT

Evaluation of the thermohydrological conditions near high-level nuclear waste packages is needed for the design of the waste canister and for overall repository design and performance assessment. Most available studies in this area have assumed that the hydrologic properties of the host rock are not changed in response to the thermal, mechanical or chemical effects caused by waste emplacement. However, the ramifications of this simplifying assumption have not been substantiated.

We have studied dissolution and precipitation of silica in thermally driven flow systems, including changes in formation porosity and permeability. Using numerical simulation, we compare predictions of thermohydrological conditions with and without inclusion of silica redistribution effects. Two cases were studied, namely, a canister-scale problem, and a repository-wide thermal convection problem and different pore models were employed for the permeable medium (fractures with uniform or non-uniform cross sections). We find that silica redistribution does not have a sizable effect on host rock and canister temperatures, pore pressures, or flow velocities.

1. INTRODUCTION

Emplacement of high-level nuclear wastes in water saturated rock formations will give rise to the development of a hydrothermal convection system, in which fluid flow is driven by buoyancy force. It was pointed out by a multidisciplinary panel convened by the Lawrence Berkeley Laboratory, that in such systems numerous processes can occur which couple thermal, hydrologic, chemical, and mechanical effects (Panel Report, 1984). The panel report identified a number of processes which may give rise to significant four-way coupling under the conditions expected near high-level nuclear waste repositories. These fully coupled processes can be broadly grouped as follows: (1) Redistribution of minerals, with associated porosity and permeability changes; (2) hydrothermal alteration of rocks and backfill; and (3) piping, or enlargement of flow channels with significant contributions from physical and mechanical effects, such as erosion of rock surfaces and selective abrasion of solid particles.

The present paper considers a particular case of redistribution of rock minerals, namely, the dissolution, transport, and precipitation of silica in the form of quartz in thermally driven flow. We are specifically interested in predicting porosity changes from silica redistribution and associated effects on permeability for nuclear waste repositories in saturated formations (Pruess and Verma, 1985). A study of a similar problem for the partially saturated tuff formations at the Nevada Test site was recently undertaken by Braithwaite and Nimick (1984).

The solubility of silica in subcritical conditions depends primarily on temperature. Groundwater flowing towards regions of higher temperature is deficient in silica, and will dissolve silica-containing rock minerals along the flow path. Conversely, water flowing towards cooler regions will generally be supersaturated and silica precipitation will take place along the flow path. In the context of nuclear waste isolation, it is not the redistribution of silica as such which is of concern, but its potential impact on the transport of

heat, fluid, and chemical constituents. (Possible effects on the mechanical properties of the rock were not considered in the present study.) The hydrologic impacts of silica redistribution are brought about by changes in formation porosity and permeability due to silica dissolution or precipitation. Dramatic effects of silica redistribution on rock porosity and permeability have been observed in laboratory experiments (Morrow et al., 1981; Moore et al., 1981; Keith et al., 1983; Vaughan, 1985).

The porosity changes caused by silica redistribution can be easily related to precipitated or dissolved mass, but the permeability change associated with this change in porosity is a much more complex problem, as the porosity-permeability correlations depend on many geometric factors such as: pore-size distribution, pore shapes, and connectivity. Since there is a wide variation in these geometric properties among natural rock formations, the porosity-permeability correlations will generally depend on the rock type and will be site specific. We have derived several correlations for different pore shape and size distributions in idealized permeable media, which are believed to capture essential features of real systems (see section 3).

In the present study we have considered both a room scale problem (which was previously considered, without including silica redistribution effects, by Pruess and Bodvarsson, 1982) and a repository scale problem. Under suitable approximations, these models were converted to two-dimensional axisymmetric models and coupled thermal, hydraulic, and chemical flow fields were numerically simulated. The results indicate that the effects of silica redistribution on the canister and the host rock temperatures, and on formation porosity and flow velocity, are generally insignificant. The only noticeable impact of silica redistribution was on permeability enhancement of the formation rock in the immediate vicinity of the canister hole. This phenomenon results in increased flux of formation water (by up to 30% over reference case) into the storage room and the canister hole.

2. MODELING APPROACH

The simulations presented in this study were carried out with the aid of the numerical code *MULKOM* (Pruess, 1983), which was developed at Lawrence Berkeley Laboratory for modeling of multi-phase, multi-component fluid and heat flow in porous and fractured media. The version of *MULKOM* used here accounts for water in liquid and vapor form and for both dissolved and solid silica, the latter being represented as quartz polymorph. All phases and the rock formations are assumed to be in local thermal equilibrium. Our code has the capability to handle finite rates of quartz dissolution and precipitation (i.e., kinetics), but in the simulations reported below we have assumed that dissolved silica concentrations correspond to equilibrium quartz solubilities, as given by Fournier and Potter (1982). The reasons for choosing a local equilibrium model for quartz dissolution and precipitation are two-fold: (1) Fluids near high-level nuclear waste repositories may contain significant amounts of dissolved minerals, so that it appeared questionable whether the available data on the kinetics of quartz dissolution and precipitation for pure water (Rimstidt and Barnes, 1980) would be applicable. Furthermore, we have no basis for estimating reaction areas per unit volume for quartz dissolution/precipitation in potential host formations for nuclear waste repositories. (2) Initial exploratory studies led us to expect that effects of silica redistribution on the thermohydrological conditions near high-level nuclear waste repositories should be minor. Assuming instantaneous local equilibrium for dissolved silica will provide a conservative (upper) limit on the amount of material dissolved or precipitated in a certain rock volume per unit time. This, in turn, will provide a conservative estimate on expected porosity and permeability changes, and on the overall thermohydrologic impact of silica redistribution.

The mass balance equations for water and silica, and the energy balance equation can all be written in the following general form.

$$\frac{d}{dt} \int_{V_n} M^{(k)} dV = \int_{\sigma_n} \mathbf{F}^{(k)} \cdot \mathbf{n} d\sigma + \int_{V_n} Q^{(k)} dV \quad (1)$$

The accumulation terms are written as follows:

$$\text{water (k=1): } M^{(1)} = \phi (S_l \rho_l + S_v \rho_v) \quad (2a)$$

$$\text{silica (k=2): } M^{(2)} = \tilde{\phi} S_s \rho_s + \phi (S_l \rho_l X_l^{(2)} + S_v \rho_v X_v^{(2)}) \quad (2b)$$

$$\text{heat (k=3): } M^{(3)} = [(1 - \tilde{\phi}) \rho_R C_R + \tilde{\phi} S_s \rho_s C_s] T + \phi (S_l \rho_l u_l + S_v \rho_v u_v) \quad (2c)$$

Here $\tilde{\phi}$ is "gross" porosity, comprising "active" porosity ϕ and the volume of solid silica (quartz) per unit formation volume. "Active" porosity represents the void volume, per unit formation volume, available to the fluid phase. This term will be referred to as "porosity" to be consistent with traditional nomenclature. S_s denotes the fraction of volume in $\tilde{\phi}$ occupied by quartz. We have the following relationship between active porosity and volume of quartz:

$$\phi = \tilde{\phi} (1 - S_s) \quad (3)$$

Thus dissolution or precipitation of quartz (changes in S_s) will produce changes in porosity ϕ , which in turn will change formation permeability, k . ρ_l , ρ_v , ρ_s , and ρ_r are the densities of liquid, vapor, quartz, and rock formation phases, respectively. C_s and C_R are quartz and rock specific heats, and u_l , u_v are specific internal energies of liquid and vapor. $X_l^{(2)}$ and $X_v^{(2)}$ are the mass fractions of dissolved silica in liquid and vapor phases. The expressions for mass flux of water and heat flux are identical to those used by Pruess and Narasimhan (1985), and need not be repeated here. Mass flux of dissolved silica is expressed in terms of liquid and vapor phase fluxes as

$$F^{(2)} = F_l X_l^{(2)} + F_v X_v^{(2)} \quad (4)$$

Thermophysical properties of liquid water and vapor are computed from the equation of state formulation given by Haar et al. (1979), with the exception of viscosity which is obtained from the correlation provided by the International Formulation Committee (1967). The densities of water and silica are assumed additive, i.e., the volume of water or vapor containing dissolved silica is assumed equal to that of pure water or vapor at

the same conditions of pressure and temperature.

The governing equations as given above are highly non-linear and strongly coupled due to variable fluid properties, relative permeabilities, phase transformation effects, and the dependence of permeability upon porosity. The equations are discretized in space with the integral finite difference method, using first order forward finite differences. All flux terms are handled fully implicitly, and are 100% upstream weighted. The resulting set of coupled non-linear algebraic equations is solved by means of Newton-Raphson iteration. The linear equations obtained at each iteration step are solved with a sparse version of LU-decomposition (Duff, 1977).

3. POROSITY-PERMEABILITY RELATIONSHIP

In modeling the complex interplay and feedback between the temperature field, rates of fluid flow, and silica redistribution, the relationship between porosity and permeability plays a crucial role. Attempts to obtain this relationship by many investigators have produced results which differ considerably from each other. For example, while Mavis and Wilsey (1937) have found the permeability (k) to be proportional to ϕ^5 or ϕ^6 , Graham (1973) found the permeability to be proportional to $(\phi - \phi_c)^{1.8}$ for sintered metallic powders, where ϕ_c represents the critical porosity at which the permeability reduces to zero. Yet another investigator (Brace, 1977) found a 3rd power correlation for crystalline rocks. It is therefore obvious that no simple general correlation between porosity and permeability can be applied to all permeable materials because this relationship depends on many complex factors such as geometric details of the pores, their sizes, and their connectivity.

However, what is needed in the current study is not an absolute permeability-porosity correlation but the relationship between their relative changes. Many investigators have proposed such relationships for different materials where the porosity changes were brought about by different physical mechanisms. For example, Lund (1974) and McClure et al. (1979) proposed an exponential relationship for permeability enhancement of sandstone due to acidizing. Pearson (1976) proposed a similar relationship for permeability enhancement of rock in geothermal reservoirs, where the porosity changes are brought about by dissolution of rock minerals in a hydrothermal flow field. Camp (1964) proposed the use of the Kozeny-Stein equation in the field of water filtration. This equation is basically a third-power relationship scaled by a factor depending on the net change in porosity. Graham's (1973) equation can be written to correlate relative changes in porosity to corresponding changes in permeability, thus, representing a 1.8th power relationship for cases where porosity alterations are caused by grain bonding in the sintering process of metallic powders. Wyble (1958) conducted an experimental

study on the effects of confining pressure on porosity and permeability for three different types of sandstones and presented his results correlating pressure to porosity and permeability reductions. His results can be restated, by factoring out pressure, to provide a porosity-permeability correlation of the form:

$$\frac{k - k_c}{k_o - k_c} = \left\{ \frac{\phi - \phi_c}{\phi_o - \phi_c} \right\}^\tau \quad (3.1)$$

where k_c and ϕ_c represent asymptotic values of permeability and porosity, which are the lowest values to which these parameters can be reduced by increasing the confining pressure and k_o , ϕ_o , and τ represent, respectively, the initial permeability, porosity, and the exponent of the correlation (determined experimentally). The study indicates that while ϕ_c was approximately $0.9\phi_o$ for all the sandstones, k_c and τ were different for different sandstones ($0.315 k_o \leq k_c \leq 0.6k_o$, and $0.73 \leq \tau \leq 1.978$). We believe that the different functional form of all these relationships are not only due to differences in pore parameters discussed above, but also due to the different mechanisms of porosity change. For example, porosity reduction under stress will primarily affect the wider portion of pores (pore bodies). Therefore, it will cause less of a permeability reduction than a comparable change in porosity from mineral precipitation, which may strongly affect the narrow portions of pores (pore throats).

We have considered highly idealized models of permeable media to correlate the relative changes in permeability to the relative changes in porosity caused by mineral redistribution. The medium is assumed to have a set of non-intersecting flow channels with either circular tubular or planar cross sections (Fig. 1). The rate of change of a tube radius (or fracture aperture) due to silica redistribution is obtained under suitable assumptions in Appendix-A. These results are subsequently used in Appendix-B to obtain permeability-porosity relationships for three different flow channel size distributions. The results for the straight capillary models (Fig. 1.a and 1.b) for the three different flow-channel size distributions (Table 1) are presented in Table 2.

The straight capillarie models (Fig. 1.a and 1.b) have been frequently employed in the literature to provide relationships between porosity and permeability changes, and usually an additional simplification was made that all flow-channels were identical (Keith et al., 1983; Braithwaite and Nimick, 1984; Vaughan, 1985; Lichtner, 1985). These "uniform channel" models fail to account for what we consider an essential feature of "real" permeable media, namely, that along a flow channel the cross section of the channel will in general be highly variable. Flow channels may contain numerous "bottlenecks" (or pore throats), so that it is conceivable that rather minor changes in average porosity may cause drastic permeability changes due to closure of the pore throats. Examples of this kind of behavior have recently been observed in laboratory experiments, in which a mere 8% reduction in original porosity resulted in 96% reduction in permeability of a granitic rock core (Vaughan, 1985). We have constructed "series models" (see Appendix-B and Figures 1.c and 1.d) which are able to represent pore throat effects. These models replicate the converging-diverging feature of the flow channels occurring in most natural permeable media. It is due to this feature that the permeability of a medium reduces to zero at a finite porosity, ϕ_c . We shall refer to this porosity as "critical porosity."

The porosity-permeability relations obtained in this study were used to perform a sensitivity analysis of the dependence of porosity-permeability relationships on the flow channel parameters discussed above. Figures 2 and 3 show the plots of permeability reduction factor (k/k_o) against normalized porosity θ , defined in Equation B.16, for fracture and tube models respectively. The upper curves in Figures 2 and 3 are for series models having identical (i.e., all the flow channels have the same geometric shape and size) flow channels with $\Gamma=0.8$ and $\frac{\bar{b}}{b}$ (or $\frac{\bar{r}}{r}$) = 3. The results for other series models, composed of flow channels of equal size having different values of Γ and $\frac{\bar{b}}{b}$ (or $\frac{\bar{r}}{r}$) than the ones mentioned above plot within a few line widths of this curve. The results for all

other models, eg. the straight flow channel models and the series models with non-identical flow channels (i.e., the flow channels within a given model differ in size according to a characteristic distribution) plot below this curve, indicating that the series model with identical flow channels represents the lower bound on permeability reduction (i.e., the smallest reduction in permeability). A similar analysis shows that the upper bound on permeability reduction is obtained for straight flow channels (i.e., $\phi_c = 0$) having the semi-Gaussian distribution shown parametrically in Table 1. Since the difference between the upper bound and the lower bound is not "large" in either the tubular or the planar flow channel case, it can be concluded that the permeability reduction factor is a relatively "weak" function of flow channel size distribution. Upon comparing Figure 2 and 3 we find that, (i) permeability reduction factor depends on the shape of flow channel cross section, and (ii) permeable media with planar flow channels experience a larger reduction in permeability for identical reduction in θ . However, the differences are not very significant over a wide range of θ ($0.3 < \theta \leq 1.0$).

The effects of irreducible porosity (ϕ_c) on permeability reduction factor is graphically presented in Figure 4, which presents permeability reduction factors for three different models. "Cubic model" refers to the model in which all the flow channels are straight, planar, and have equal apertures. The other two curves are for two different series models in which all the flow channel are planar and identical, i.e., the probability density function is represented by a Delta function ($h(b) = \delta(b)$). These curve show that irreducible porosity has a very significant effect on permeability reduction function and, in fact, it is the most important parameter in determination of permeability reduction functions for natural permeable media where ϕ_c is expected to be large ($\phi_c \geq 0.8$).

In the current study we have used three different porosity-permeability relationships; namely, simple cubic ($\phi_c = 0$), series with $\phi_c = .8$, and series with $\phi_c = 0.95$, which are discussed above and plotted over a limited range in Figure 4. The latter case was

chosen to explore effects of an extremely strong dependence of permeability upon porosity changes. Note that the change in slope at $\phi/\phi_0 = 1$ is due to a change in horizontal scale at this point.

4. CASES STUDIED

We have evaluated silica redistribution effects for a room-scale model previously studied by Pruess and Bodvarsson (1982), and for a repository-scale model.

4.1 Room-Scale Model

This model represents a 2-D axisymmetric approximation for a symmetry element of a reference repository design from the BWIP project. The approximations and assumptions behind this model have been discussed in detail in a report by Pruess and Bodvarsson (1982). The geometric layout of the flow system is shown in Figure 5. A linear string of 8.5 waste packages is placed at the axis of a cylinder of 19.9 m radius, at the mantle of which ambient boundary conditions of $T = 57.3^\circ\text{C}$ and $p = 130$ bars are maintained. The hole containing the waste packages is connected to a portion of a drift ("room"), which is represented as a cylinder of 5.97 m radius and 3.03 m height. Before backfill, the room is open for approximately 50 years with the pressure in the room maintained at $p = 1$ bar. The computational grid is shown in Figure 6 and is identical to the "coarse mesh" used by Pruess and Bodvarsson (1982). Other problem specifications for the room scale model are given in Tables 3 and 4.

4.2 Repository-Scale Model

In this problem, the repository is idealized to be a flat circular disk with a given time-varying power density. The repository is assumed to be 1500 m in radius and situated in a fully saturated rock mass 900 m below the ground surface (Figure 7). The axi-symmetric mesh used for numerical computation is shown in Figure 8. The top of the model is bounded by an isothermal impermeable surface 150 m below the ground level, at 10°C and corresponding hydrostatic pressure. The bottom surface is impermeable and at 85°C corresponding to a $30^\circ\text{C}/\text{km}$ ambient geothermal gradient. The lateral boundary is maintained at constant pressure and temperature corresponding to

ambient hydrostatic pressure gradient and ambient geothermal gradient respectively. Regional flow is ignored.

In order to reduce the numerical effort, it is assumed that the entire repository is instantaneously loaded with 10 year old spent fuel and filled to an areal power density of 22 W/m^2 . The effects of the pressure sink in the storage tunnel is also ignored because resaturation is expected to take place within a short time (~ 100 years) compared to the time period of regional fluid movement ($\sim 10,000$ years).

The repository parameters used in the present study are presented in Table 5. Although the current study was not intended to be representative of any particular waste-isolation site, the lithology and the formation properties shown in Figure 8 and Table 5, respectively, are for the BWIP site in Hanford (DOE Report, 1982). No distinction is made between the waste canister, backfilled material and the repository host rock. The power density is assumed to decline with time, corresponding to spent-fuel (Figure 9).

5. RESULTS

The results of this study are presented in two parts, one each for the room-scale model and the repository-scale model. Since the physical phenomena pertaining to the performance assessment of a nuclear waste repository are different at these two scales, a qualitative description of the phenomenology is given before the numerical results. This will facilitate presentation of the numerical results and clarify the approach used in the simulation.

5.1 Room-Scale Model

5.1.1 General Phenomenology

The case studied by Pruess and Bodvarsson (1982) without silica redistribution will be referred to as "reference case". We will quote Pruess and Bodvarsson (1982) for the description of the reference case before discussing the effects of silica redistribution:

"It is assumed that the waste packages are emplaced "hot"; at a temperature of 300 °C. In low permeability rocks, most of the heat generated by the canisters is removed by thermal conduction. After emplacement in a relatively cool (54 °C) host rock, canister temperatures initially decline, but, within a few days, heat loss to the rock decreases to a level below the rate of heat generation in the canisters. Subsequently, both temperatures and temperature gradients increase everywhere in the system, with the largest increases occurring in the immediate vicinity of the canister storage hole. About two years after emplacement, temperature gradients have increased to the point where all generated heat is being removed from the canisters. This causes canister temperatures to first stabilize, and then to slowly decline as heat output diminishes.

At greater distance from the canister storage hole, temperatures remain lower, and maximum temperatures are reached somewhat later.

Prior to backfilling, canister storage holes and storage rooms are close to atmospheric pressure (1 bar), while groundwater pressure at the depth of the reference horizon is approximately 130 bars (13 MPa). This causes pore fluids to migrate toward the pressure sink (canister holes and storage rooms). Due to the small compressibility of liquid water, the pressure pulse diffuses rapidly outward, away from storage rooms and canister holes, and reaches the boundaries of the low-permeability zone in a matter of days. Subsequently, a quasi-steady flow field is maintained throughout the open period of the repository, with water influx at the boundary of the low permeability zone closely matching discharge into the excavations."

As water flows towards the excavations, temperature and silica solubility generally increase. Therefore, the water flowing into a pore space is always deficient in silica with respect to the local solubility, and local equilibrium is achieved by dissolution of silica from the rock mass. Dissolution of silica results in an increase in flow rate because of the enhanced permeability. However, the flow increase causes secondary effects which tend to diminish the impact: an increased flow rate tends to reduce the temperature along the flow path, thus diminishing the fluid mobility because of higher fluid viscosity at lower temperatures.

When the permeability enhancements are very large near the canister holes, a low pressure front propagates rapidly into the rock surrounding the canister holes. If the pressure drops below the saturation pressure, boiling occurs and the resulting two-phase zone acts as an additional barrier to the flowing fluid because of the relative permeability effects.

5.1.2 Thermal and Hydrologic Effects

For the reference case and the new case studied with inclusion of silica redistribution effects, the total fluid flow into the storage room and the canister hole essentially equals total fluid flow at the boundary of the model at all times. This demonstrates that quasi-steady flow conditions are present at all times due to low fluid compressibility, and the slow rates of changes in the temperature field. The changes in total flow rate with time for all four models are illustrated in Figure 10. The figure indicates that for the reference case the flux initially increases due to reduced viscosity of the heated fluid. Later, as the thermal output from the canisters decreases, the temperature in the rock decreases and the flow diminishes. The figure also indicates that redistribution of silica enhances the maximum fluid flow rates by up to 20% with respect to the reference case. To fully understand this phenomenon one needs to examine the temperature variations brought about by redistribution of silica.

Figure 11 illustrates the temperature history at two different locations in the rock mass for the reference case and the series model with $\phi_c = 0.95$. The results of the other two studies fall within these limits, with the cubic case being closer to the reference case and the series model with $\phi_c = 0.8$ being closer to the series model with $\phi_c = 0.95$. Figure 12 illustrates the temperature profiles at 10 and 30 years after emplacement. These two figures illustrate that redistribution of silica causes the rock temperature to reduce everywhere at all times. However, the differences are generally small ($\leq 10^\circ\text{C}$ over most of the flow system).

Upon reexamining Figure 10 one can conclude that silica redistribution brings about two counteracting phenomena affecting the fluid flow: the formation permeability is increased and the fluid mobilities are decreased with respect to the reference case. The net result is an enhancement of flow because the former effect is dominant.

An inflection in the flow rate for the series model with $\phi_c = 0.95$ at approximately 28 years is caused by boiling in the rock mass (see Fig. 10). The presence of two-phase

conditions presents a larger flow resistance due to relative permeability effects. After disappearance of the steam phase at approximately 28 years, the flow rate rises again and reaches a plateau at approximately 44 years.

Porosity enhancement for the series model with $\phi_c = 0.8$ at two different times is presented in Figure 13. The results of the two other models fall within 0.008 of this curve and they are tabulated in Table 6. This observation at first seems counterintuitive in light of large flow-rate differences among the three models considered in this study. But the observation seems plausible when one considers the fact that higher flow rates result in lower temperature rise and temperature gradients.

5.1.3 Boiling in the Rock Mass

It was found in a previous study (Pruess and Bodvarsson, 1982) that a very fine spatial resolution is required near the canister hole in order to predict the exact (very small) extent of boiling two-phase zones. However, because of the high cost of numerical computation on a "fine mesh," only a "coarse mesh" calculation was carried out here, so that the extent of boiling is underestimated in this study.

It is because of this reason that no boiling was observed in the reference case, the cubic model, and the series model with $\phi_c = 0.8$. But, steam phase appears in the first ring of rock elements surrounding the canister hole for a series model with $\phi_c = 0.95$ (actual extent of boiling is probably larger). One may therefore conclude that the extent of boiling in the cubic model and the series model with $\phi_c = 0.8$ is bounded by the boiling zones observed by Pruess and Bodvarsson (1982) in their "fine mesh" simulation of the reference case without silica redistribution effects, and the series model with $\phi_c = 0.95$.

The "fine mesh" calculations of the reference case (Pruess and Bodvarsson, 1982) show that the maximum rock volume in which boiling occurs is 0.46m^3 per canister.

This value is reached 10 months after emplacement, at which time boiling extends to a radial distance of 13.2 cm beyond the wall of the canister hole. The rock mass thus desaturated is resaturated in 44 years, before the assumed backfilling and decommissioning of the repository.

Table 7 compares the extent of boiling in the reference case and the series model with $\phi_c = 0.95$. From the Table 7 we can see that silica redistribution effects tend to enlarge the two-phase zone, and to reduce the resaturation time. These changes are brought about because dissolution of silica enhances the permeability primarily near the canister hole, and therefore causes low pressures to advance further into the rock mass. This reduces the pressure to the saturation pressure at local temperatures over a larger region. Enhanced permeability also causes faster resaturation, because of overall increased fluid flow rates.

5.2. Repository-Scale Model

5.2.1. General Phenomenology

It is assumed that the entire repository is loaded at once and that there are no pressure sinks within the repository. Since a repository is expected to receive waste over a few decades and resaturation is expected to take place within 100 years, the impact of the above-mentioned assumptions on a simulation study for up to 10,000 years is expected to be negligible. Heating of the repository and its surroundings due to radioactive decay of the waste causes a natural convection cell to develop in which flow is driven by the buoyancy force of the heated water relative to the surrounding colder water. In this convection cell, water moving towards the repository generally moves towards higher temperatures, thus dissolving silica along its flow path. Upon leaving the repository, the point of maximum temperature, the silica-enriched water moves towards lower temperature and solubility, and precipitation of silica along the flow channel takes

place. This phenomenon will, in general, result in an overall increase in flow resistance in a medium with homogeneous permeability.

Porosity and permeability changes are not only brought about by silica redistribution on a macroscopic scale, but also by local changes in solubility due to changing temperature. When the temperatures in the repository and the host rock rise due to waste emplacement, silica from the flow channel walls dissolves, resulting in increased porosity and permeability. When the temperature declines these effects are reversed.

5.2.2 Flow and Temperature Field

Figure 14 displays the temperature vs. depth profile along the axis of the repository for the reference case (no silica), at different times after waste emplacement. The initial undisturbed temperature profile is a straight line, representing a normal geothermal gradient of $30^{\circ}\text{C}/\text{km}$. At early times the temperature rise is localized near the repository horizon. After approximately 1000 years, heat from the repository reaches the top of the formation and begins to leak out. Radially, the temperature is fairly uniform within the radius of the repository, beyond which the temperature drops sharply. The effects of silica redistribution on these temperature profiles are so small that a plot will fall within a line's width of the reference plot.

A comparison of the temperature histories of the repository center for the reference case and the series model with $\phi_c = 0.95$ is shown in Figure 15. It shows that silica redistribution results in somewhat lower repository temperature, but the differences are $\leq 7^{\circ}\text{C}$ at all times, which is not significant. Redistribution of silica also has an insignificant effect on the flow velocities (Table 8). The results indicate that at early times (~ 100 years) redistribution causes a reduction in flow. However, at later times (≥ 500 years) the effects are reversed because the local dissolution dominates over the changes brought about by non-isothermal flow.

6. CONCLUSIONS

We have studied effects of silica redistribution in thermally driven flow fields near high-level nuclear wastes emplaced in saturated rocks, both on a room scale and a repository-wide scale. Our studies are not necessarily indicative in a quantitative sense of the effects to be expected at the various potential repository sites currently under consideration. However, we believe that some general conclusions can be drawn.

Silica redistribution will tend to increase effective formation permeability and fluid migration velocities, while diminishing formation temperatures near the canister holes. None of these effects appear to be significant and of any concern, especially when viewed against general uncertainties in applicable formation parameters at any specific site. For example, changes in predicted temperatures from silica redistribution effects are generally below 10° C everywhere except in the immediate vicinity of the waste packages, where somewhat larger effects appear possible. These conclusions were arrived at on the basis of conservative assumptions, which tend to overpredict thermohydrological effects of silica redistribution. Specifically we mention the assumption of instantaneous local equilibrium for dissolved silica concentrations, and the very severe porosity-permeability relationship used here which accounts for permeability effects of pore-throats and bottle necks in flow channels.

From the viewpoint of assessing thermohydrological conditions, and migration of dissolved species near a high-level nuclear waste repository in saturated rock, our results suggest that effects of silica redistribution may be safely ignored. However, near nuclear waste packages emplaced in partially saturated media conditions may be different. It is possible that "heat pipe" conditions with persistent liquid-vapor counterflow may evolve (Pruess and Wang, 1984), which could cause substantial amounts of mineral redistribution in the near-canister region.

APPENDIX A: MINERAL REDISTRIBUTION IN FLOW CHANNELS

We discuss the time dependence of mineral dissolution or deposition in a flow channel due to non-isothermal flow. The assumptions and restrictions invoked in this study are:

- (i) flow is one dimensional, Darcian, and quasi-steady, i.e., the flow rate is constant over a finite macroscopic flow channel length and changes very slowly compared to any change in temperature;
- (ii) flow-rate is small, and dispersion of dissolved minerals in the flow channel is negligible;
- (iii) there exists a local thermal and chemical equilibrium between the solution and the porous matrix; mineral concentrations in the fluid correspond to the local solubility;
- (iv) the matrix is rigid; and
- (v) the deposition or dissolution is uniform over a macroscopic flow channel length.

Under the assumptions listed above, the relationship between porosity and permeability will not depend on the applied boundary conditions. It is convenient to consider boundary conditions of constant pressure, because in this case all flow channels act independently. (For boundary conditions of constant total flow rate all flow channels are coupled, as deposition will cause a rate change in one channel to be compensated by simultaneous rate changes in all other channels.)

We write the basic mass balance equation for deposition or dissolution of mineral component i in a flow channel in the following form

$$\rho_i \frac{dA}{dt} = q \rho_w c_i \quad (\text{A.1})$$

where A is the cross-sectional area of the flow channel, q is the volumetric flow rate, and $c_i' = dc_i/dx$.

We consider two types of flow channels, namely, plane fractures and straight cylindrical tubes (Figure 1). For fractures, the relationship between pressure gradient and volumetric flow rate per unit fracture width is given by the "cubic law" (Witherspoon et al., 1979)

$$q_f = - \frac{b^3}{12} \frac{\nabla p}{\mu} \quad (\text{A.2})$$

where b is the fracture aperture.

For tubes, the corresponding relationship is the Hagen-Poiseuille equation (Scheidegger, 1974)

$$q_t = - \frac{\pi}{8} r^4 \frac{\nabla p}{\mu} \quad (\text{A.3})$$

where r is the tube radius.

For fractures, $A = b \cdot 1$ (aperture times unit width), so equations (A.1) and (A.2) can be combined to obtain

$$\rho_i \frac{db}{dt} = \frac{-b^3 \rho_w}{12\mu} p' c_i' \quad (\text{A.4})$$

For quasi-steady conditions, the time variations of ρ_w and c_i' can be neglected and equation (A.4) can be integrated yielding

$$b = \frac{b_o}{\sqrt{1 + \gamma b_o^2}} \quad (\text{A.5})$$

where

$$\gamma = \frac{\rho_w}{6\rho_i\mu} c_i' p' t.$$

For tubes, $A = \pi r^2$, so equations (A.1) and (A.3) can be combined to obtain

$$\rho_i \frac{d(r^2)}{dt} = -\frac{r^4 \rho_w}{8\mu} p' c_i' , \quad (\text{A.6})$$

which can be integrated to yield

$$r = \frac{r_o}{\sqrt{1 + \eta r_o^2}} \quad (\text{A.7})$$

where

$$\eta = \frac{\rho_w}{8\rho_i\mu} c_i' p' t.$$

APPENDIX B: POROSITY-PERMEABILITY RELATIONSHIPS FOR IDEALIZED PERMEABLE MEDIA

From Equation (A.2), the effective continuum permeability of a set of plane, parallel, infinite fractures with aperture b and fracture density N_f is seen to be

$$k_f = \frac{N_f b^3}{12} \quad (\text{B.1})$$

while the porosity is given by

$$\phi_f = N_f b \quad (\text{B.2})$$

For a set of straight, parallel, infinite tubes with radius r and a density of N_t tubes per unit cross sectional area, the effective continuum permeability is from Equation (A.3)

$$k_t = \frac{N_t \pi}{8} r^4 \quad (\text{B.3})$$

while the porosity is given by

$$\phi_t = N_t \pi r^2 \quad (\text{B.4})$$

The time dependence of b and r due to mineral redistribution are given by equations (A.5) and (A.7), respectively. By combining equations (B.1) and (B.2), or equations (B.3) and (B.4) the following expressions for permeability as an explicit function of porosity can be obtained.

$$k_f = \frac{\phi_f^3}{12 N_f^2} \quad (\text{B.5})$$

and

$$k_t = \frac{\phi_t^2}{8\pi N_t} \quad (\text{B.6})$$

Let us now consider permeable media with a size distribution of fracture apertures or tube radii (Figures 1a and 1b). Quantitatively a distribution can be specified by a

probability density function $h(b)$ (or $h(r)$), where $h(b)db$ represents the fraction of flow channels with apertures in an interval db around b . For a system of straight, parallel fractures, the continuum porosity and permeability are given by

$$\phi_f = N_f \int_0^{b_{\max}} b h(b)db \quad (B.7)$$

$$k_f = N_f \int_0^{b_{\max}} \frac{b^3}{12} h(b)db \quad (B.8)$$

For a system of straight, parallel, cylindrical tubes, the corresponding equations are

$$\phi_t = N_t \int_0^{r_{\max}} \pi r^2 h(r)dr \quad (B.9)$$

$$k_t = N_t \int_0^{r_{\max}} \frac{\pi r^4}{8} h(r)dr \quad (B.10)$$

If mineral deposition takes place, all fracture apertures (or tube radii) will change with time, so that the corresponding probability density function, along with porosity and permeability, will become time-dependent. In general, depending upon spatial and temporal variability of applied boundary conditions, apertures (or radii) could change in a very complex way. Here we are interested in developing relationships between porosity and permeability change suitable for applications in numerical modeling. For this purpose it is appropriate to assume that within each volume element, flow channels of the same aperture (or radius) experience the same amount of deposition, and furthermore, that the deposition is uniform along the flow channel. All fractures with apertures in an interval db_0 around b_0 at time t_0 will have apertures in an interval db around b at a later time t , so that

$$h_0(b_0) db_0 = h(b(t)) db \quad (B.11)$$

Equation (B.11) shows the parametric dependence of the probability density function upon time and it can be solved explicitly by substituting $b = b(b_0, t)$ from Equation

(A.5). Completely analogous relationships hold for the radii of tubular flow channels where dependence of a tube radius on time is given by Equation (A.7). Expressions for porosity and permeability changes in a rock mass having different flow channel size distributions, given in Table 1, are listed in Table 2.

The above discussion was made for flow channels with uniform cross sectional areas. In many permeable media flow channels consist of "wide" and "narrow" segments (corresponding to pore bodies and pore throats), whose lengths are of the order of a pore diameter. We shall here develop a simple model for such media, as schematically depicted in Figures (1c and 1d). Let us assume that a fraction Γ of the total length of a capillary tube has a radius \bar{r} , while the remainder $1 - \Gamma$ has a smaller radius r . Assuming all tubes to be identical, and rate of deposition to be uniform, the porosity-permeability relationship can be obtained by considering the case of single tube per unit area. Initial porosity ϕ_o and permeability k_o are given by

$$\phi_o = \pi \{ \Gamma \bar{r}^2 + (1 - \Gamma)r^2 \} \quad (B.12)$$

$$\frac{1}{k_o} = \frac{8}{\pi} \left\{ \frac{\Gamma}{\bar{r}^4} + \frac{1 - \Gamma}{r^4} \right\} \quad (B.13)$$

If a volume Λ is deposited per unit length, porosity becomes $\phi = \phi_o - \Lambda$. The flow channel will become completely clogged and permeability will go to zero when $\Lambda = \pi r^2$, at which time we still have a finite porosity $\phi_c = \phi_o - \pi r^2$. Denoting the radii of the tube segments after deposition of Λ by \bar{r}_α and r_α , respectively, the porosity and permeability are given by

$$\phi = \pi [\Gamma \bar{r}_\alpha^2 + (1 - \Gamma) r_\alpha^2] \quad (B.14)$$

$$\frac{1}{k} = \frac{8}{\pi} \left\{ \frac{\Gamma}{\bar{r}_\alpha^4} + \frac{1 - \Gamma}{r_\alpha^4} \right\} \quad (B.15)$$

Introducing the normalized porosity

$$\theta = \frac{\phi - \phi_c}{\phi_o - \phi_c} \quad (B.16)$$

with $\phi_c = \pi\Gamma(\tilde{r}^2 - r^2)$ and the ratio of cross sectional areas of the tube segments, $\omega = \left(\frac{\tilde{r}}{r}\right)^2$, we obtain

$$\frac{k}{k_o} = \theta^2 \cdot \frac{1 - \Gamma + \Gamma/\omega^2}{1 - \Gamma + \Gamma \left(\frac{\theta}{\theta + \omega - 1} \right)^2} \quad (\text{B.17})$$

A completely analogous treatment can be made for fractures, with apertures of \tilde{b} and b , respectively, over fractions Γ and $1 - \Gamma$ of total length. We have

$$\phi_o = \Gamma\tilde{b} + (1 - \Gamma)b, \text{ and} \quad (\text{B.18})$$

$$\frac{1}{k_o} = 12 \left\{ \frac{\Gamma}{\tilde{b}^3} + \frac{1 - \Gamma}{b^3} \right\} \quad (\text{B.19})$$

The normalized porosity θ is defined as in Equation (A.16), with $\phi_c = \Gamma(\tilde{b} - b)$. Introducing

$$\nu = \frac{\tilde{b}}{b} \quad (\text{B.20})$$

we find

$$\frac{k}{k_o} = \theta^3 \cdot \frac{1 - \Gamma + \Gamma/\nu^3}{1 - \Gamma + \Gamma \left\{ \frac{\theta}{\theta + \nu - 1} \right\}^3} \quad (\text{B.21})$$

NOMENCLATURE

A	cross-sectional area
a	distribution parameter (Table 1)
b, \tilde{b}	fracture apertures
c	silica solubility
C	specific heat
d	distribution parameter (Table 1)
D	parabolic cylinder function
h	probability density function
k	intrinsic permeability
$F^{(i)}$	mass flux of component i
$M^{(i)}$	accumulation term of component i
\mathbf{n}	unit normal vector
N	flow channel density, number of flow channels per unit area
p	pressure
$Q^{(i)}$	source term for component i
q	volumetric flow rate
r, \tilde{r}	capillary tube radii
R	($= \frac{d}{a}$) distribution parameter (Table 1)
S	saturation
t	time
T	absolute temperature
u	specific internal energy
x	linear distance
X	mass fraction of silica
V	volume

Greek Symbols

α, β	dimensionless aperture (Table 1)
γ	$\frac{\rho_w}{6\rho_i\mu} c_i' p' t$
Γ	fractional length (Fig. 1)
δ	dimensionless aperture (Table 1)
η	$\frac{\rho_w}{8\rho_i\mu} c_i' p' t$
θ	normalized porosity
Λ	volume of precipitate
λ	dimensionless radius (Table 1)
μ	absolute viscosity
ν	area ratio for fracture ($=\bar{b}/b$)
ρ	density
$\tilde{\phi}$	gross porosity
ϕ	porosity ($\phi = \tilde{\phi} (1 - S_s)$)
ψ, Ω	dimensionless tube radii (Table 1)
ω	area ratio for tube, $\{ = (\frac{\bar{r}}{r})^2 \}$

Subscripts and Superscripts

c	critical values
f	fracture
i	index of mineral component
l	liquid phase
n	grid block number
o	initial condition
r	formation rock
s	solid phase silica

t tube
v vapor phase

ACKNOWLEDGEMENTS

This work was supported by the U.S. Nuclear Regulatory Commission, through NRC Fin No. B3046-3 under Interagency Agreements DOE-60-83-388 and 60-83-367, through U.S. Department of Energy Contract No. DE-AC03-76SF00098.

The authors would like to thank Joseph Wang and Cristine Doughty for reviewing the manuscript and Leslie Fairbanks for her help in preparation of the manuscript.

REFERENCES

- Brace, W. F., Permeability from Resistivity and Pore Shape, *Journal of Geophysical Research*, Vol. 82, No. 23, pp. 3343-3349, 1977.
- Braithwaite, J. W., and Nimick, F. B., Effect of Host-Rock Dissolution and Precipitation on Permeability in a Nuclear Waste Repository in Tuff, Sandia Report SAND84-0192, Sandia National Laboratories, Albuquerque, New Mexico, September 1984.
- Camp, T. R., *Theory of Water Filtration*, A.S.C.E, Sc. 4, Vol. 90, pp. 1-3, 1964.
- DOE Report, Site Characterization Report for Basalt Waste Isolation Project at Hanford, Report No. DOE/R L 82-3, prepared by Rockwell, Hanford Operations, Hanford, WA., 1982.
- Duff, I. S., MA28 - A Set of FORTRAN Subroutines for Sparse Unsymmetric Linear Equations, Report No. AERE-R-8730, Computer Sciences and Systems Division, AERE Harwell, Oxfordshire, U.K., July 1977.
- Fournier, R. O., and Potter, R. W., An Equation Correlating the Solubility of Quartz in Water from 25 °C to 900 °C at Pressures Up to 10,000 Bars, *Geochimica et Cosmochimica Acta*, Vol. 56, pp. 1969-1973, 1982.
- Graham, R. A., A Quantitative Determination of Microstructure on Gas Permeability of UO_2 and Ni Sintered Bodies, M.S. Thesis, U. of Florida, Gainesville, FL., 1973.
- Haar, L., Gallagher, J., and Kell, G. S., Thermodynamic Properties for Fluid Water, *Proceedings, 9th International Conference on Properties of Steam*, pp. 1-14, Munich, 1979.
- International Formulation Committee, A Formulation of the Thermodynamic Properties of Ordinary Water Substance, IFC Secretariat, Duesseldorf, Germany, 1967.

Keith, L. A., Delaney, P. T., and Moore, D. E., Permeability Reduction Due to Precipitation of Quartz under Nonisothermal Conditions, Proceedings, Ninth Workshop on Geothermal Reservoir Engineering, Stanford University, Stanford, CA, December 1983.

Lichtner, P. C., Continuum Model for Simultaneous Chemical Reactions and Mass Transport in Hydrothermal Systems, *Geochimica et Cosmochimica Acta*, Vol. 49, No. 3, pp. 779-800, March, 1985.

Lund, K., On Acidizing of Sandstone, Ph.D. Dissertation, U. of Michigan, Ann Arbor, MI, 1974.

Mavis, F. T., and Wilsey, E. F., *Eng. News Rec.*, Vol. 118, No. 2, 1937; as quoted by Scheidegger, 1974.

McClure, L. C., Fogler, H. S., and Kline, W. E., An Experimental Technique for Obtaining Permeability-Porosity Relationships in Acidizing Porous Media, *I. & E. C. Fund.*, Vol. 18, pp. 188-191, 1979.

Moore, D. E., Morrow, C. A., and Byerlee, J. D., § S i 0 sub 2 § Precipitation Accompanying Fluid Flow Through Granite Held in a Temperature Gradient, Proceedings, Seventh Workshop on Geothermal Reservoir Engineering, Stanford University, Stanford, CA, December 1981.

Morrow, C., Lockner, D., Moore, D., and Byerlee, J., Permeability of Granite in a Temperature Gradient, *Journal of Geophysical Research*, Vol. 86, No. 84, pp. 3002-2008, April 1981.

Panel Report on Coupled Thermo-Mechanical-Hydro-Chemical Processes Associated with a Nuclear Waste Repository, Lawrence Bekeley Laboratory Report No. LBL-18250, Berkeley, CA, 1984.

Pearson, R. O., Planning and Design of Additional East Mesa Geothermal Test Facilities (Phase 1B), 1 - Final Report, SAN/1140-1/1, ERDA, 1976.

Pruess, K., Development of the General Purpose Simulator MULKOM, Annual Report, 1982, Earth Sciences Division, Lawrence Berkeley Laboratory, Berkeley, CA, 1983.

Pruess, K., and Bodvarsson, G., Hydrothermal Conditions and Resaturation Times in Underground Openings for a Nuclear Waste Repository in the Umtanum Flow at the Basalt Waste Isolation Project, Lawrence Berkeley Laboratory Report No. LBL-18451, Berkeley, California, July 1982.

Pruess, K., and Narasimhan, T. N., A Practical Method for Modeling Fluid and Heat Flow in Fractured Porous Media, Society of Petroleum Engineers Journal, Vol. 25, No. 1, pp. 14-26, February 1985.

Pruess, K., and Verma, A., Literature Review on Coupled Thermal-Hydro-Mechanical-Chemical Effects, letter report to the NRC (unpublished), March 1985.

Pruess, K., and Wang, J. S. Y., TOUGH - A Numerical Model for Nonisothermal Unsaturated Flow to Study Waste Canister Heating Effects, in: G. L. McVay (ed.), Mat. Res. Soc. Symp. Proc., Vol. 26, Scientific Basis for Nuclear Waste Management, pp. 1031-1038, Elsevier, New York, 1984.

Rimstidt, J. D., and Barnes, H. L., The Kinetics of Silica-Water Reactions, *Geochimica et Cosmochimica Acta*, Vol. 44, pp. 1683-1699, 1980.

Scheidegger, A., The Physics of Flow through Porous Media, New York City, The Macmillan Company, 1974.

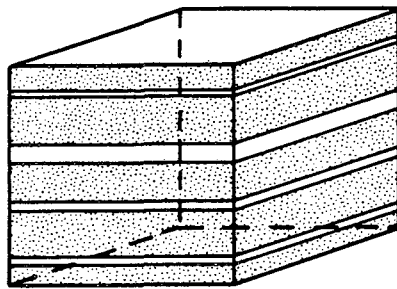
Vaughan, P. J., Analysis of Permeability Reduction During Flow of Heated, Aqueous Fluid through Westerly Granite, paper presented at Int. Symp. on Coupled Processes Affecting the Performance of a Nuclear Waste Repository, Berkeley, CA, September 18-20, 1985.

Witherspoon, P. A., Wang, J. S. Y., Iwai, K., and Gale, J. E., Validity of Cubic Law for Fluid Flow in a Deformable Rock Fracture, *Water Resources Research*, Vol. 16, No. 6, pp. 1016-1024, 1979.

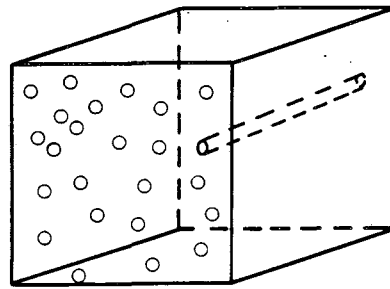
Wyble, D. O., Effect of Applied Pressure on Conductivity, Porosity and Permeability of Sandstones, Petroleum Transactions AIME, Vol. 213, pp. 430-432, 1958.

LIST OF FIGURES

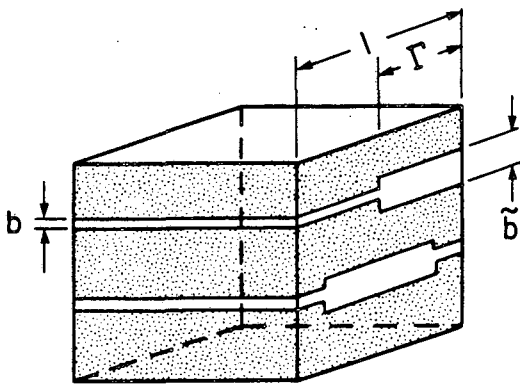
- Figure 1. Idealized models of permeable media. Figures (a) and (b) represent the straight capillare models, and figures (c) and (d) are the "series" models.
- Figure 2. Plot of permeability reduction factors for planar flow channel models.
- Figure 3. Plot of permeability reduction factors for tubular flow channel models.
- Figure 4. Porosity-permeability relationships for three different models considered in this study.
- Figure 5. Axisymmetric representation of the room-scale problem.
- Figure 6. Discretization of room-scale problem.
- Figure 7. Schematic of the axisymmetric model of the repository.
- Figure 8. Discretization of the axisymmetric repository model.
- Figure 9. Decay of the relative power density with time.
- Figure 10. History of fluid flow rates into the canister holes and storage room for room-scale problem.
- Figure 11. Variation in temperature at different locations in room-scale problem with and without inclusion of silica redistribution effects.
- Figure 12. Temperature profiles at the different times in room-scale problem with and without inclusion of silica redistribution effects.
- Figure 13. Porosity enhancement at 10 and 42 years in room-scale model ($\phi_c=0.8$).
- Figure 14. Vertical temperature profiles along the repository axis.
- Figure 15. The effects of silica redistribution on the temperature history of the repository center.



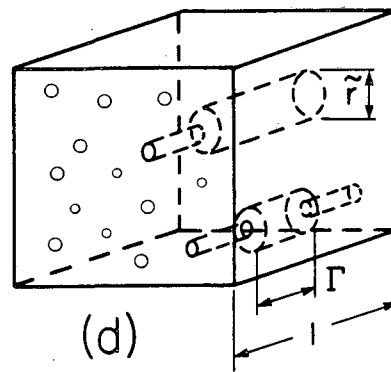
(a)



(b)



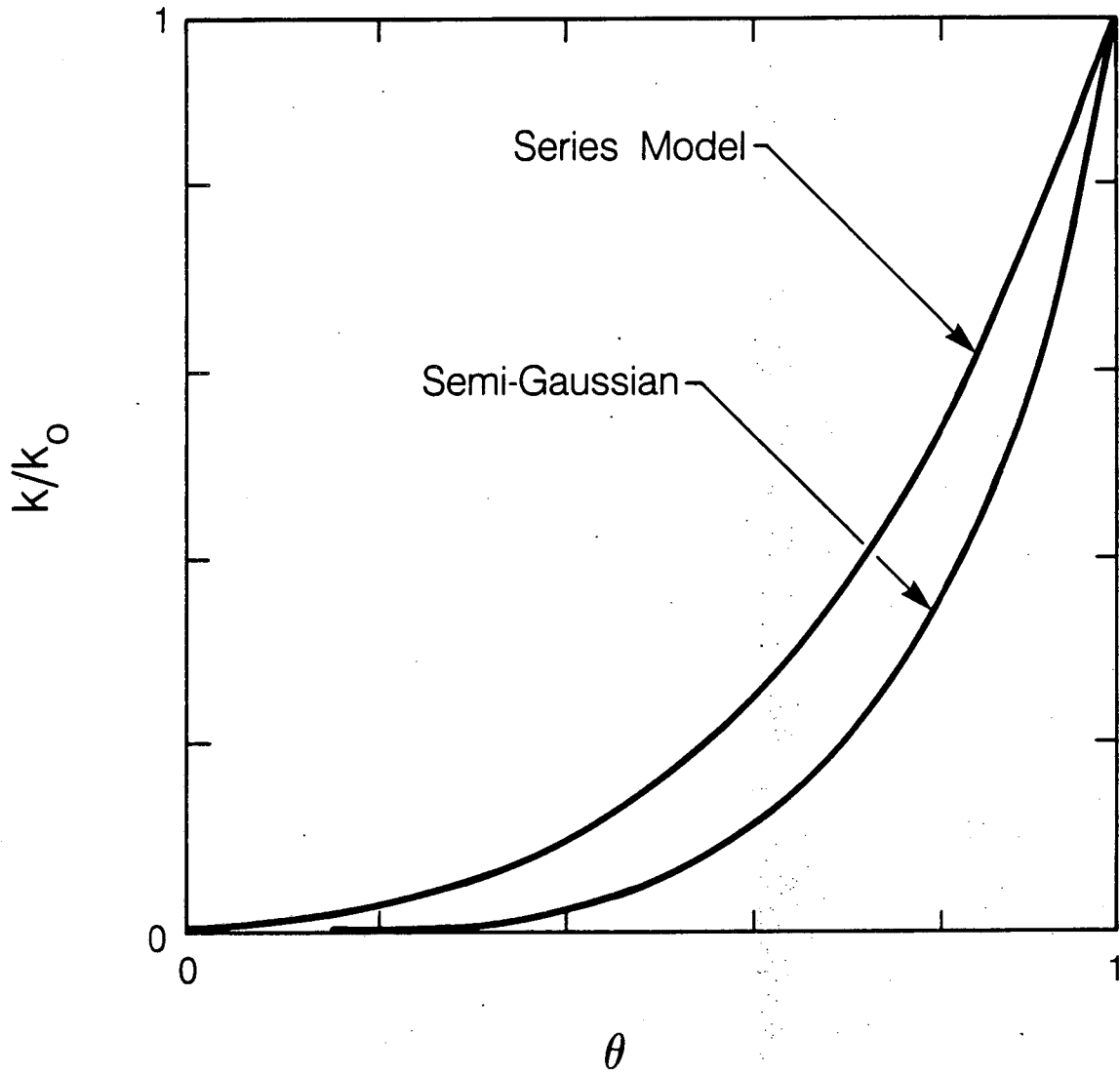
(c)



(d)

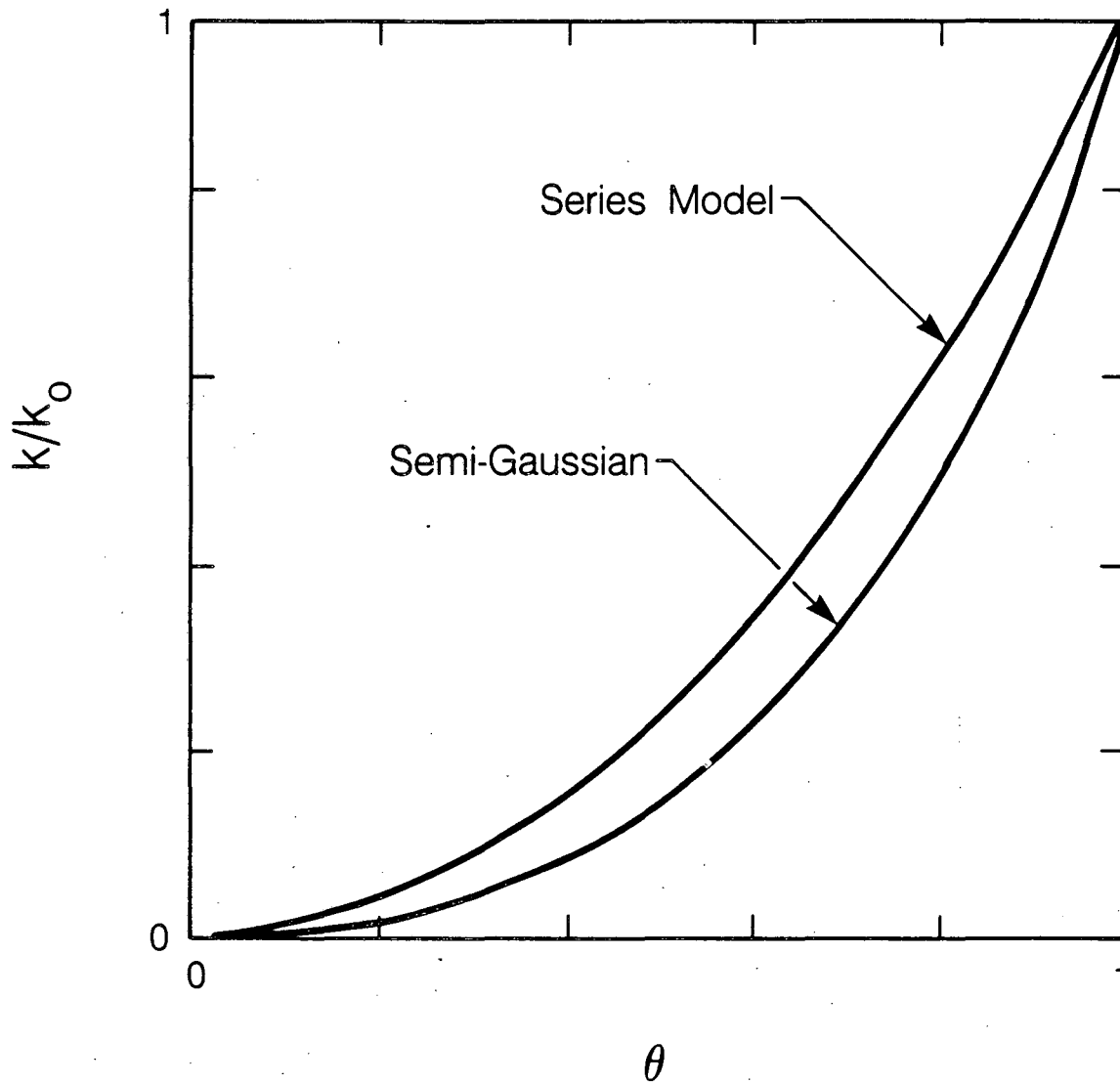
XBL 859-10773

Figure 1. Idealized models of permeable media. Figures (a) and (b) represent the straight capillary models, and figures (c) and (d) are the "series" models.



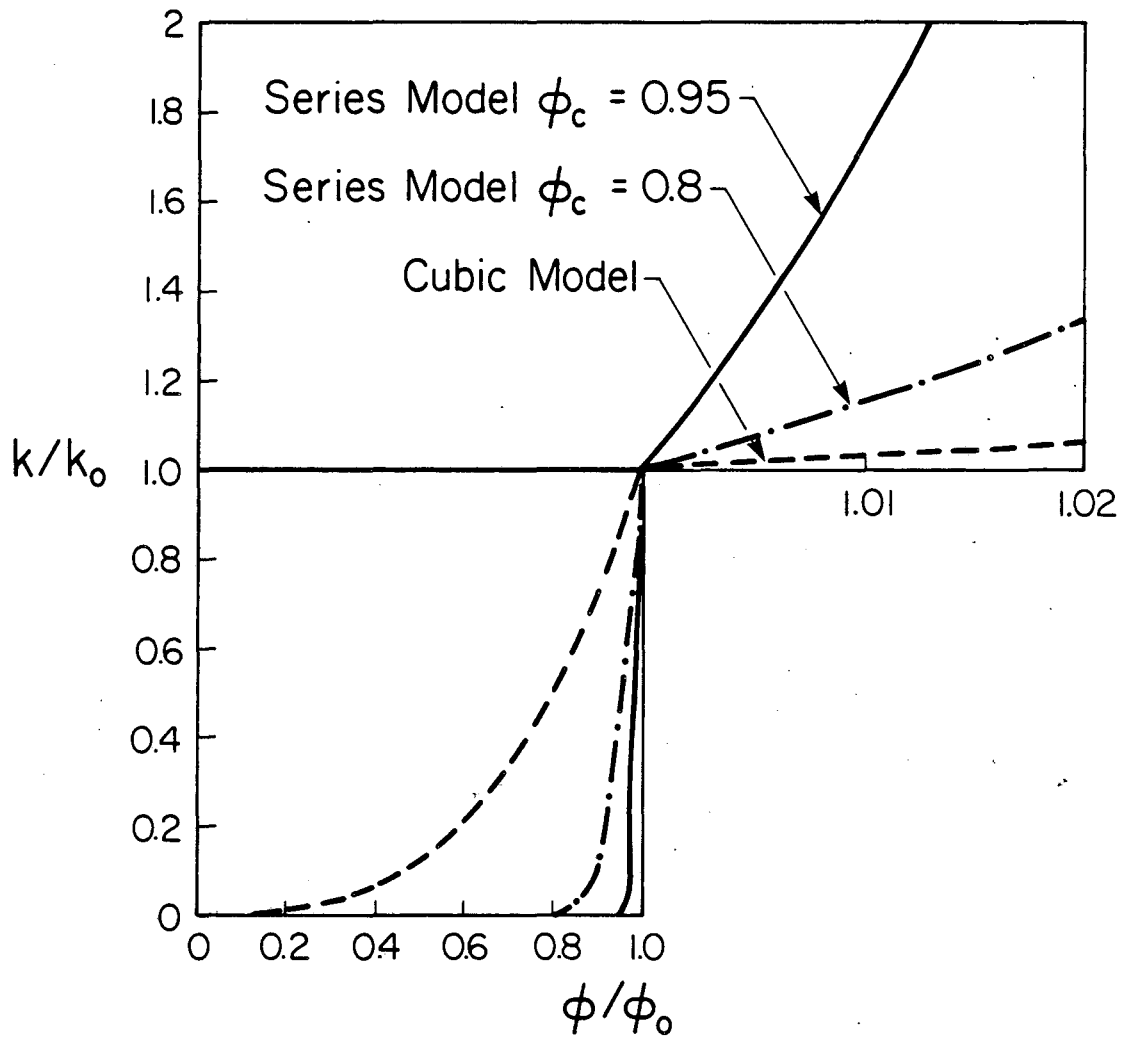
XBL 861-10471

Figure 2. Plot of permeability reduction factors for planar flow channel models.



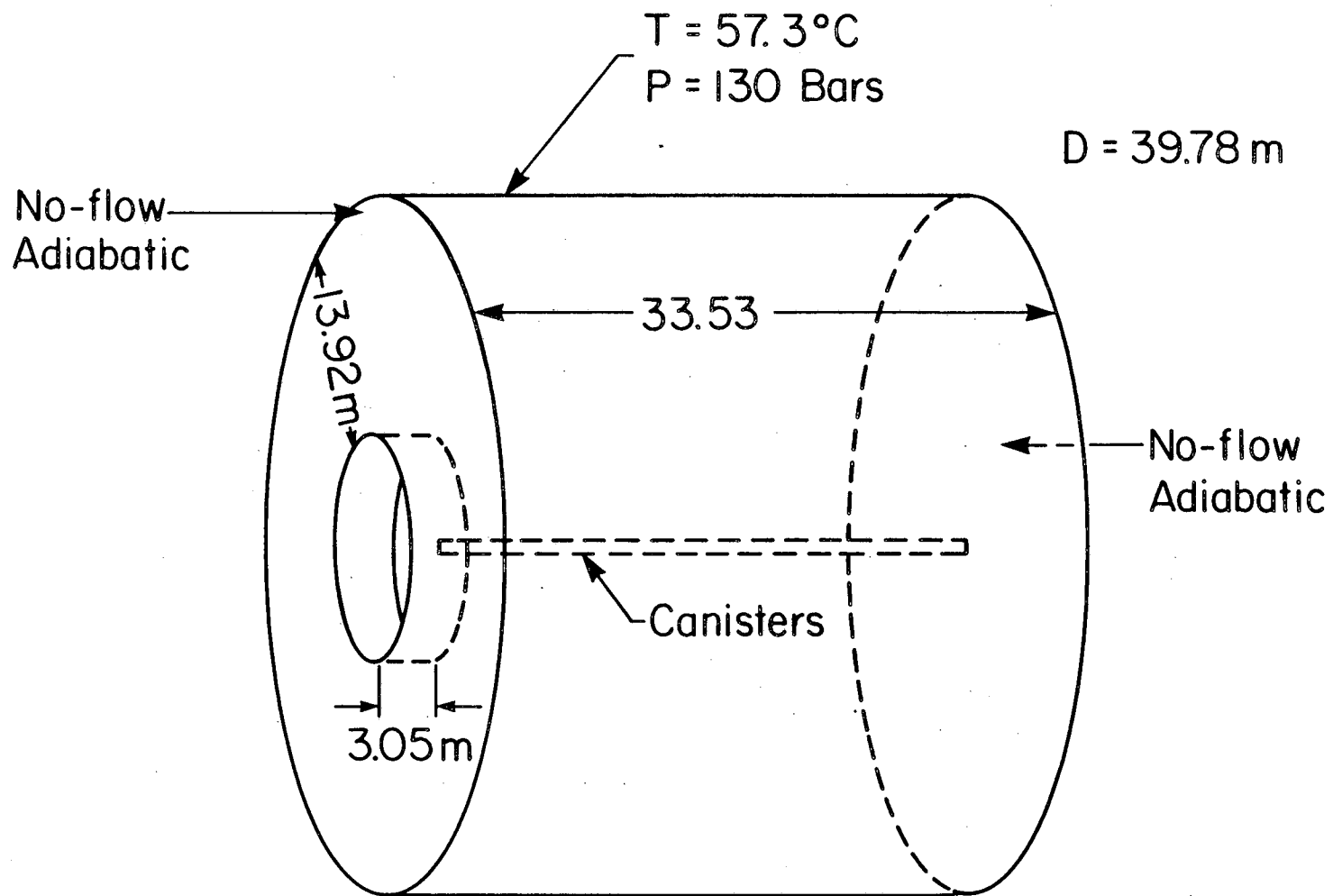
XBL 861-10470

Figure 3. Plot of permeability reduction factors for tubular flow channel models.



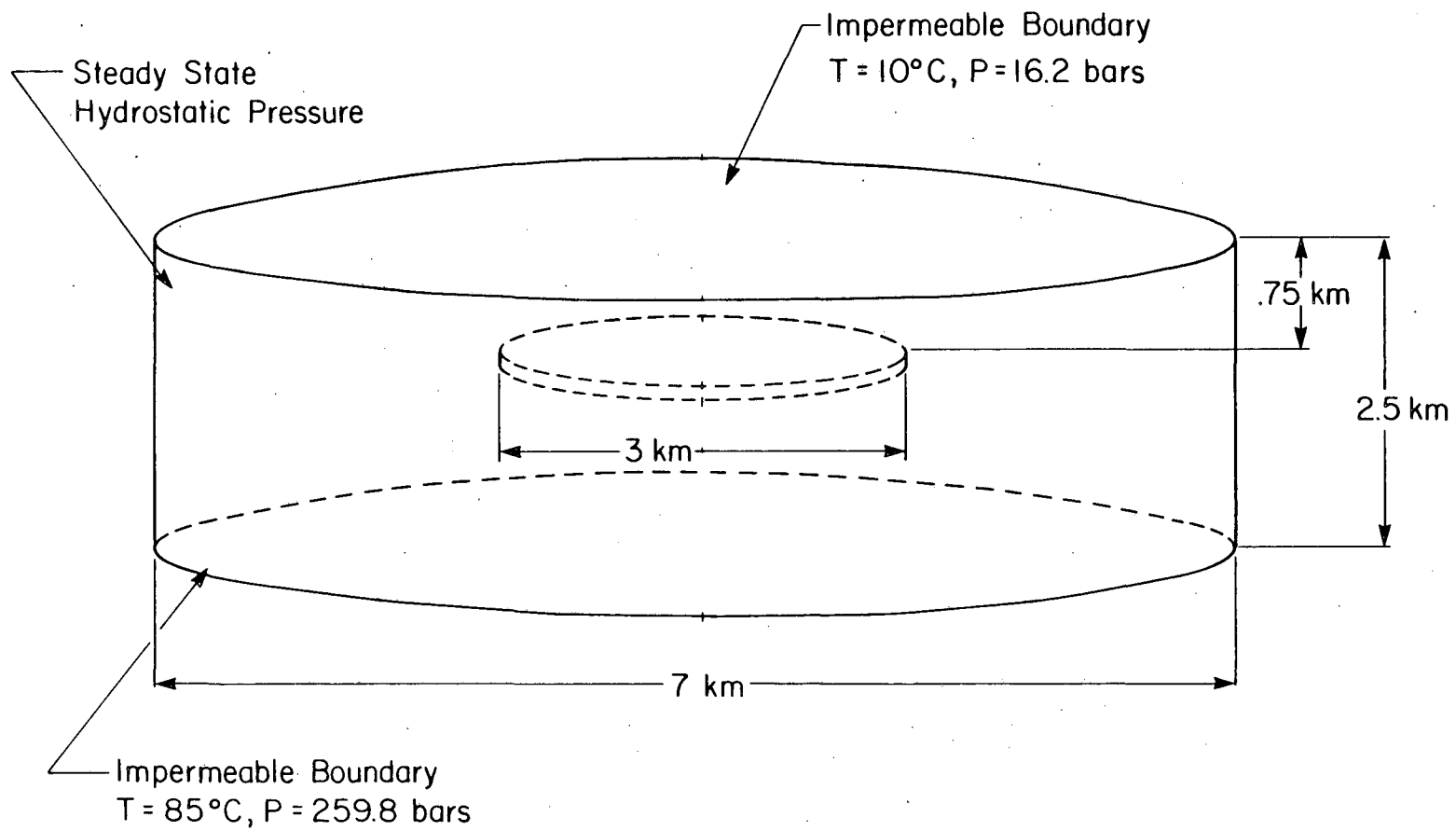
XBL 859-10761

Figure 4. Porosity-permeability relationships for three different models considered in this study.



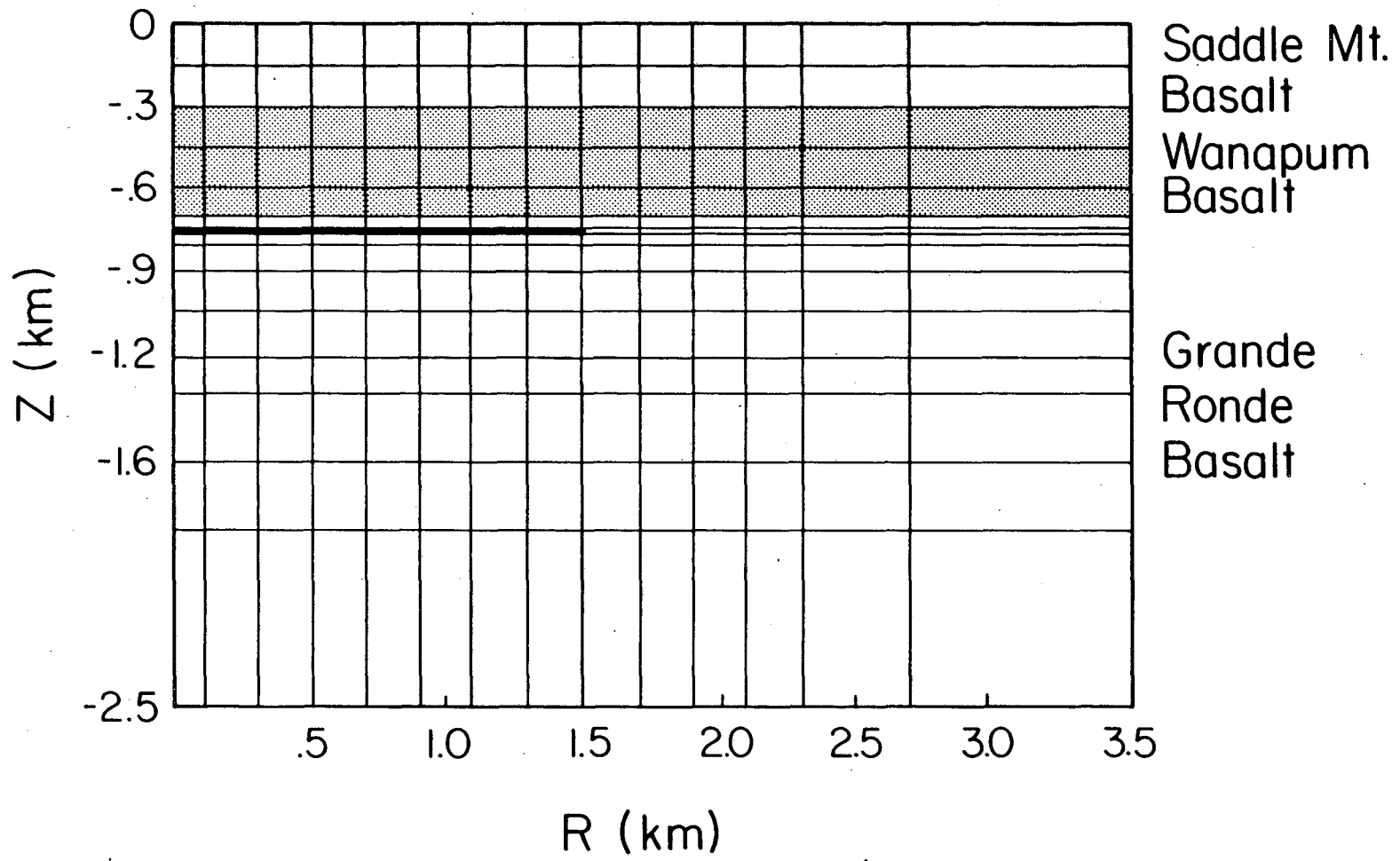
XBL 859-10771

Figure 5. Axisymmetric representation of the room-scale problem.



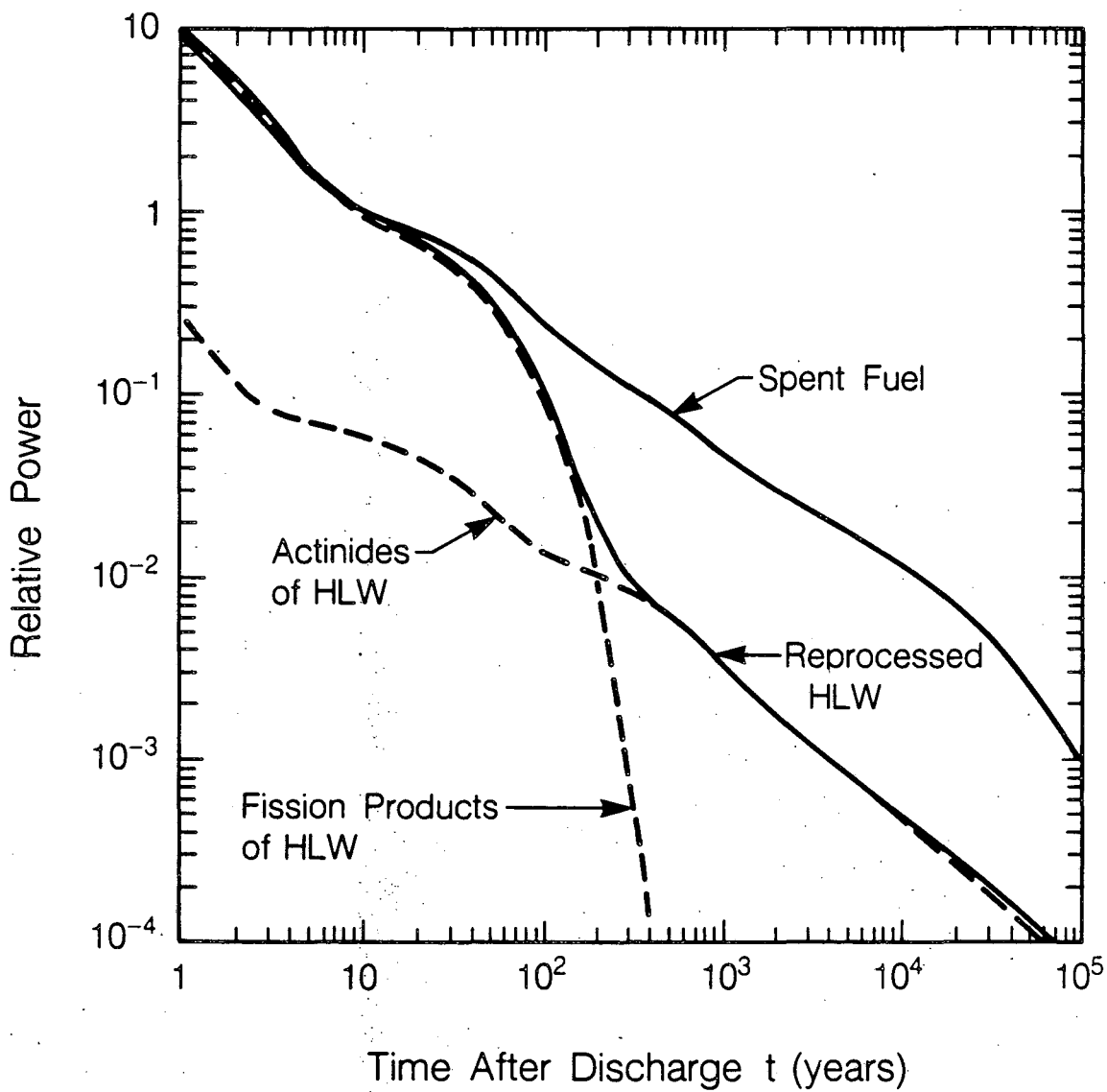
XBL 859-10772

Figure 7. Schematic of the axisymmetric model of the repository.



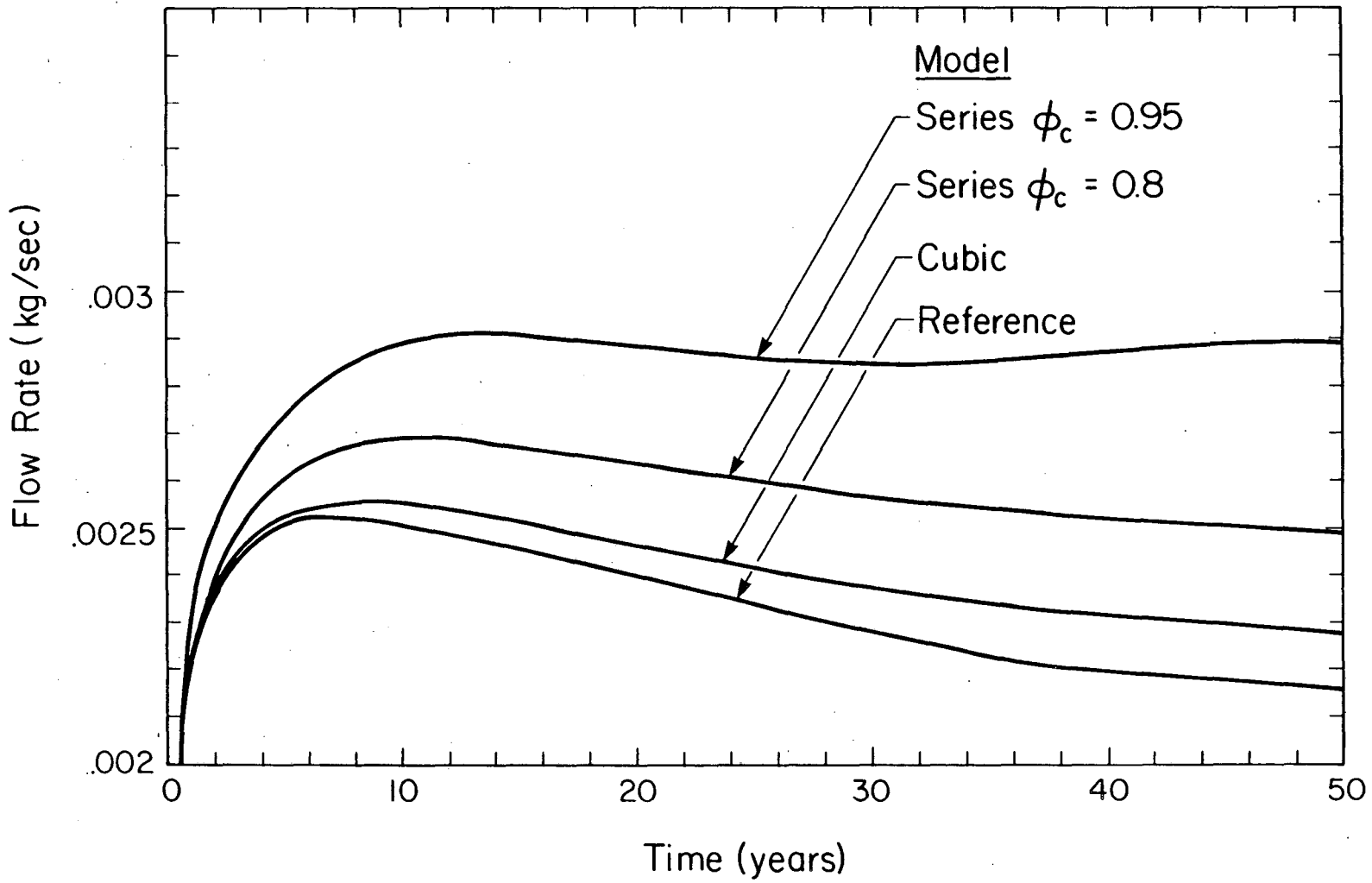
XBL 859-10770

Figure 8. Discretization of the axisymmetric repository model.



XBL 8512-12692

Figure 9. Decay of the relative power density with time.



XBL 859-10765

Figure 10. History of fluid flow rates into the canister holes and storage room for room-scale problem.

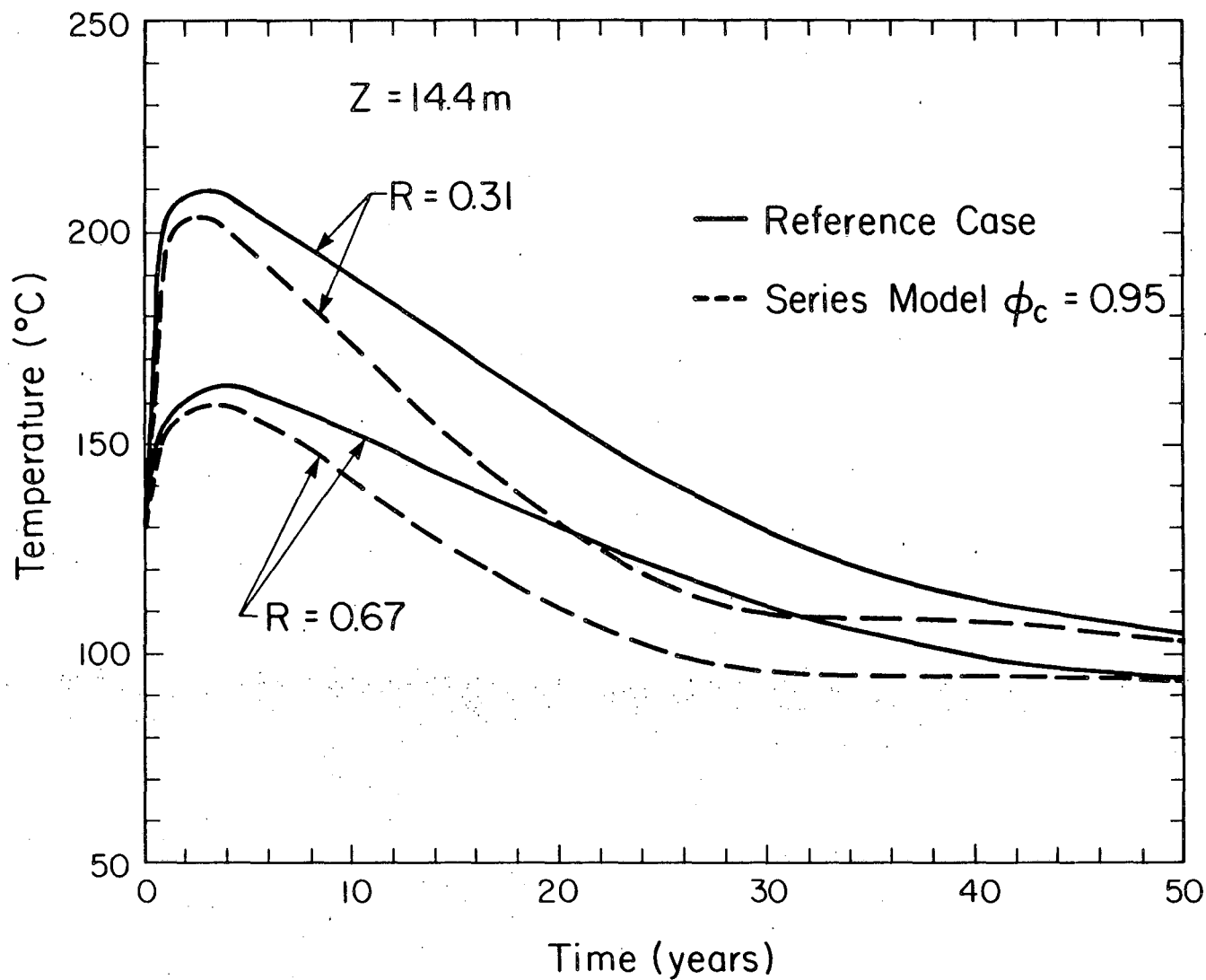


Figure 11. Variation in temperature at different locations in room-scale problem with and without inclusion of silica redistribution effects.

XBL 859-10768

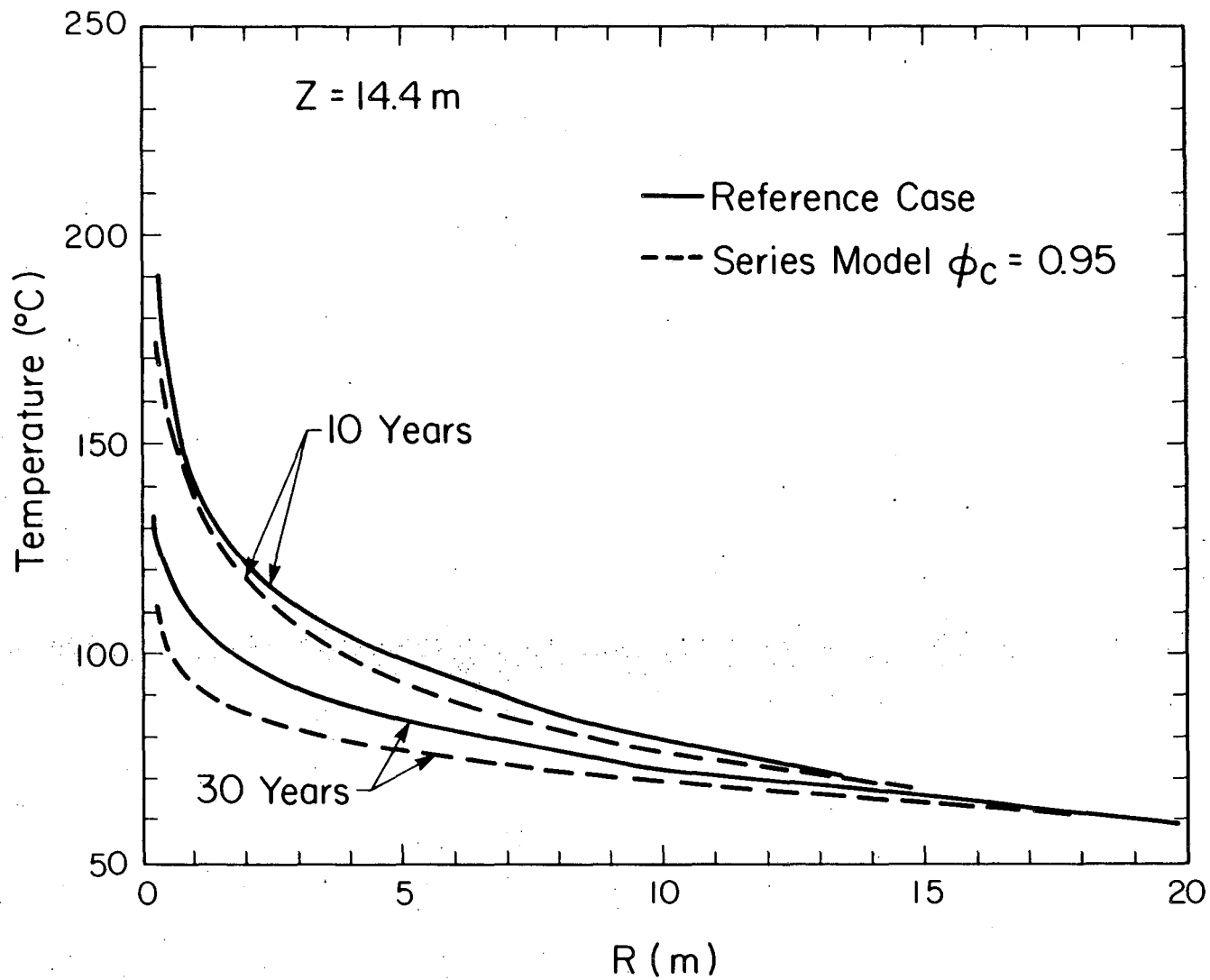
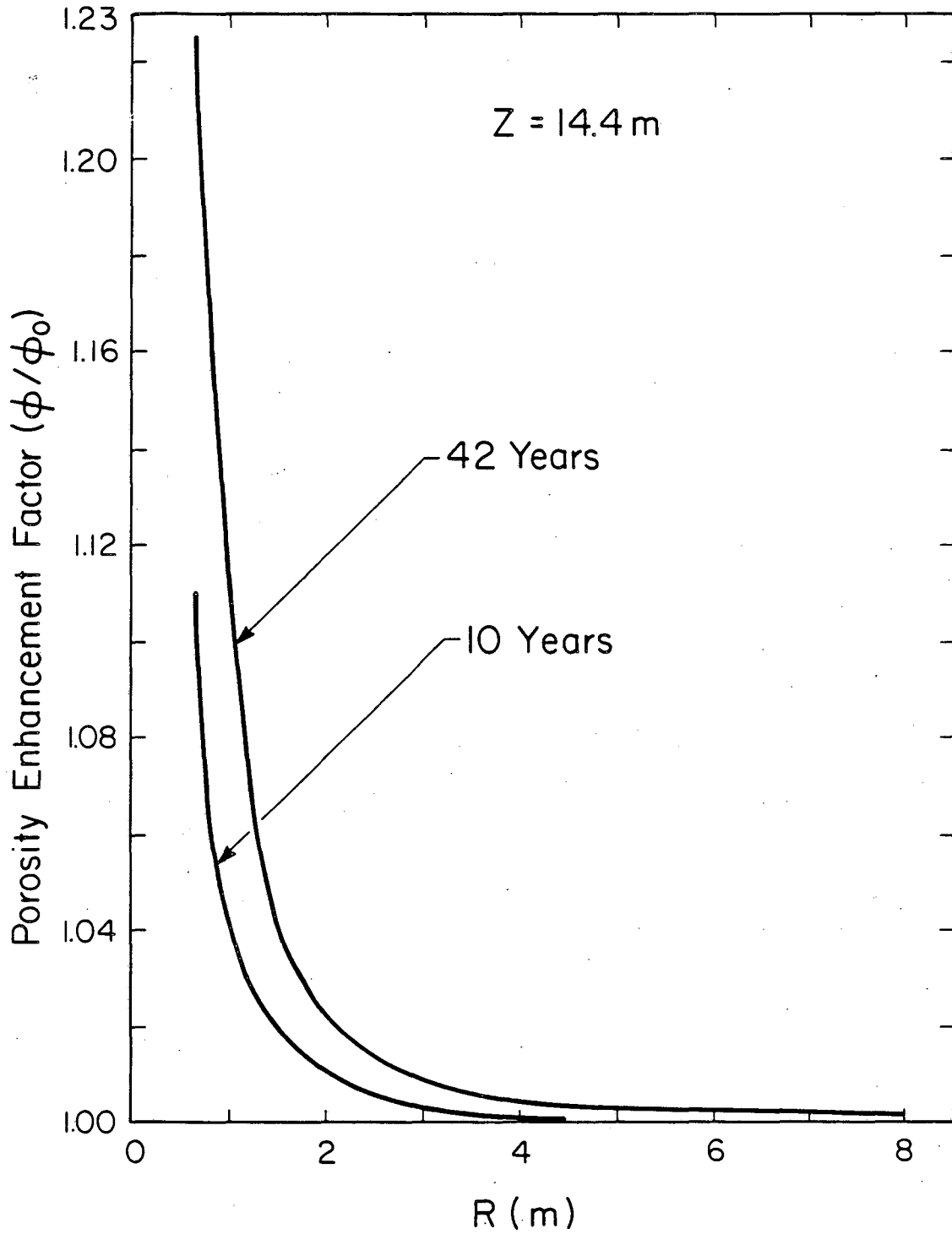


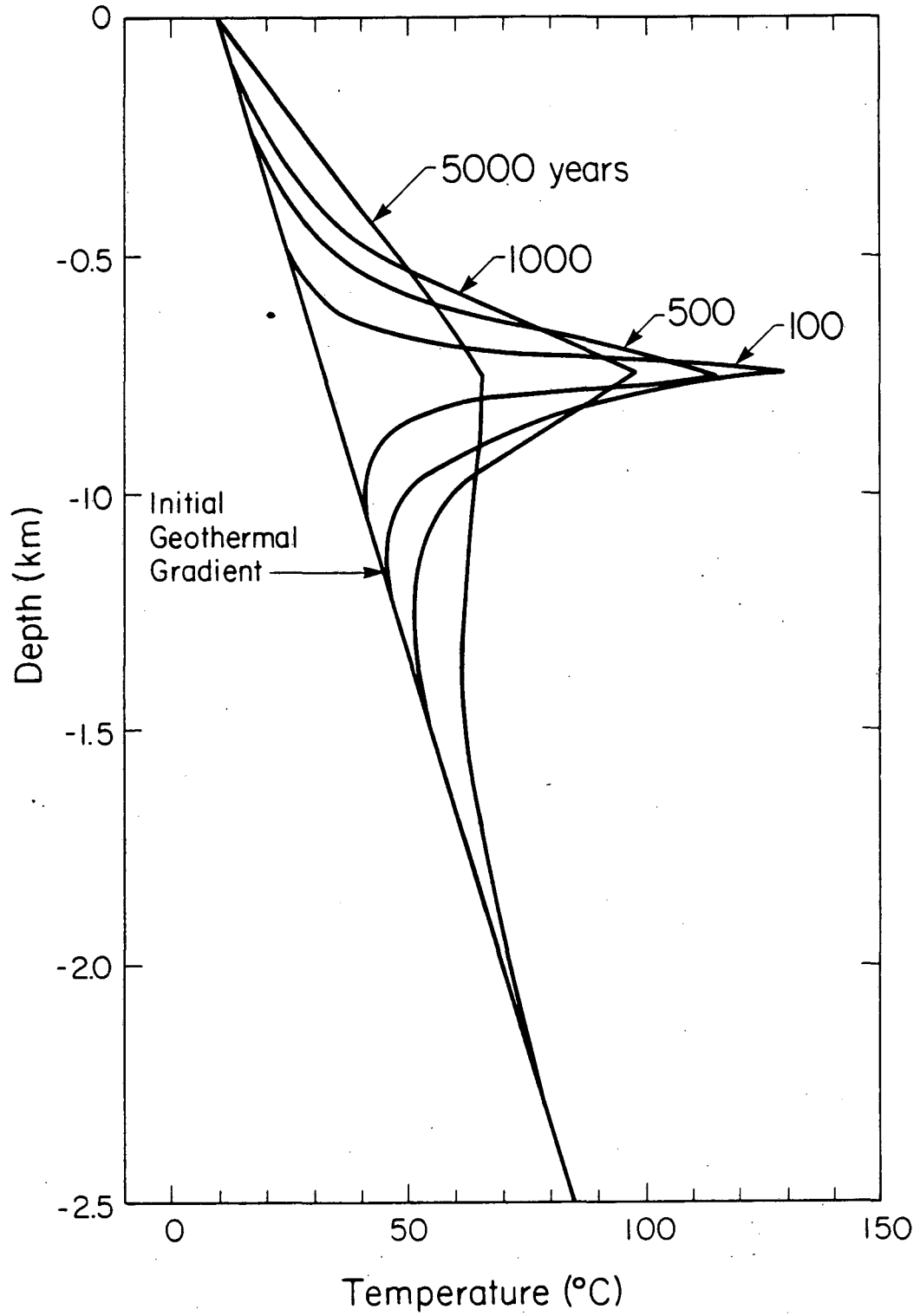
Figure 12. Temperature profiles at the different times in room-scale problem with and without inclusion of silica redistribution effects.

XBL 859-10767



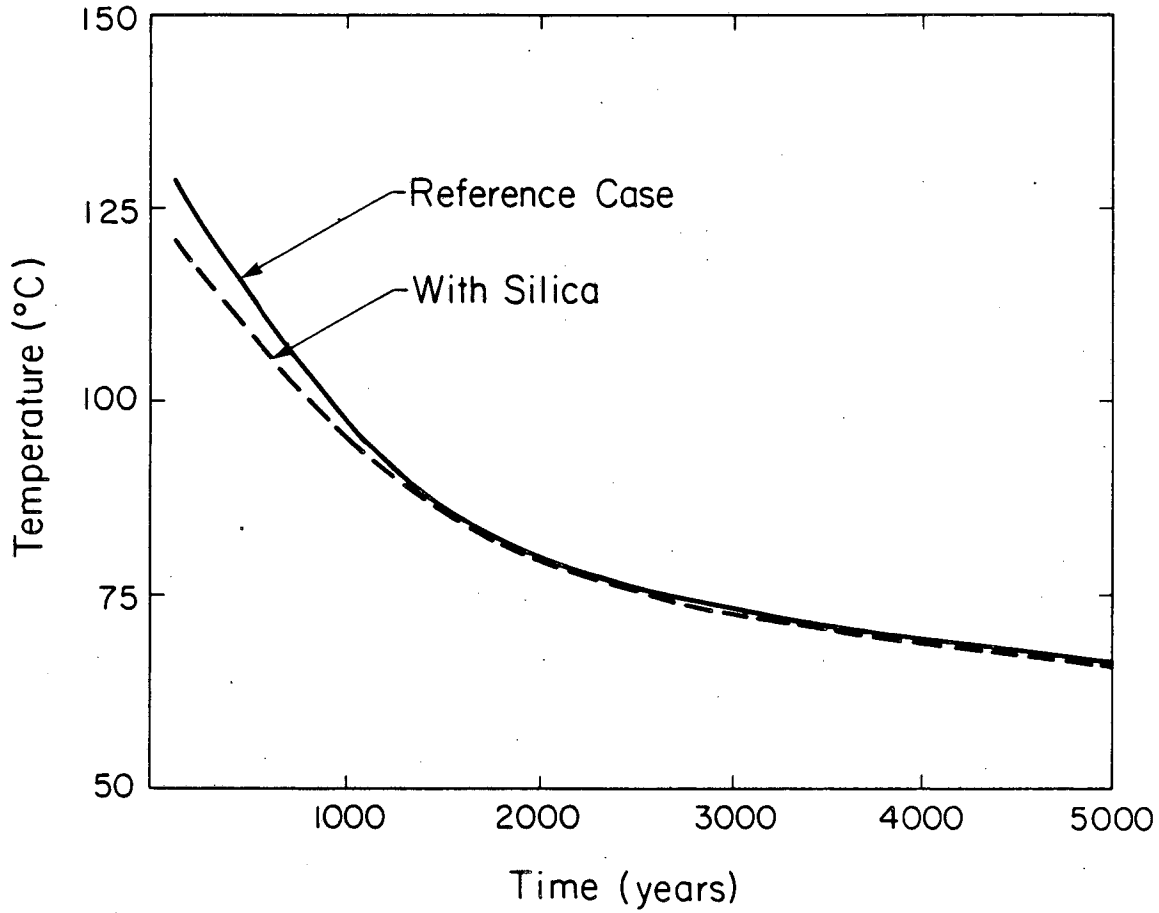
XBL 859-10766

Figure 13. Porosity enhancement at 10 and 42 years in room-scale model ($\phi_c=0.8$).



XBL 859-10762

Figure 14. Vertical temperature profiles along the repository axis.



XBL 859-10763

Figure 15. The effects of silica redistribution on the temperature history of the repository center.

LIST OF TABLES

- Table 1. Probability density functions for three different flow-channel size distributions.
- Table 2. Porosity and permeability variations for the distributions shown in Table 1 assuming the straight capillary model.
- Table 3. Parameters used in room scale problem.
- Table 4. Relative heat-generation rates of waste canisters after emplacement.
- Table 5. Parameters used in repository-wide model.
- Table 6. Relative changes in formation porosity for different porosity-permeability relationships.
- Table 7. Extent of boiling and resaturation time with and without inclusion of silica redistribution effects.
- Table 8. Vertical flow velocity along the repository axis with and without inclusion of silica redistribution effects.

Table 1. Probability density functions for three different flow-channel size distributions.

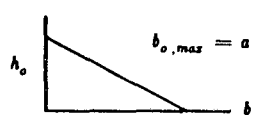
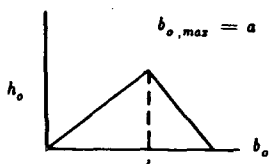
DISTRIBUTION	FRACTURE MODEL	TUBE MODEL
<p><i>Semi-Gaussian</i></p>  <p>$h_o(b_o) = \frac{2a}{\sqrt{\pi}} e^{-a^2 b_o^2}$</p>	$h(b) = \frac{2a}{\sqrt{\pi}} \exp(-a^2 b^2 / (1 - \gamma b^2) (1 - \gamma b^2)^{-3/2})$ $a = \sqrt{\phi_o / 12k_o}$ $N = \sqrt{\pi} \phi_o \sqrt{\phi_o / 12k_o}$	$h(r) = \frac{2a}{\sqrt{\pi}} \exp(-a^2 r^2 / (1 - \eta r^2) (1 - \eta r^2)^{-3/2})$ $a = \sqrt{3\phi_o / 16k_o}$ $N = 3\phi_o^2 / 8\pi k_o$
<p><i>Linear</i></p>  <p>$h_o(b_o) = \frac{2}{a^2} (a - b_o)$</p>	$h(b) = \frac{2}{a^2} \left(a - \frac{b}{\sqrt{1 - \gamma b^2}} \right) (1 - \gamma b^2)^{-3/2}$ $a = \sqrt{40k_o / \phi_o}$ $N = 3\phi_o \sqrt{\phi_o / 40k_o}$	$h(r) = \frac{2}{a^2} \left(a - \frac{r}{\sqrt{1 - \eta r^2}} \right) (1 - \eta r^2)^{-3/2}$ $a = \left\{ \frac{20k_o}{\phi_o} \right\}^{1/2}$ $N = \frac{3\phi_o^2}{20\pi k_o}$
<p><i>Triangular</i></p>  <p>$h_o(b_o) = \frac{2}{ad} b_o, 0 \leq b_o \leq d$ $h_o(b_o) = \frac{2}{a(a-d)} (a - b_o), d \leq b_o \leq a$</p>	$\frac{2}{ad} \frac{b}{(1 - \gamma b^2)^2}, 0 \leq b \leq \frac{d}{\sqrt{1 + \gamma d^2}}$ $h(b) = \frac{2}{a(a-d)} \left(a - \frac{b}{\sqrt{1 - \gamma b^2}} \right) (1 - \gamma b^2)^{-3/2}$ $\frac{d}{\sqrt{1 + \gamma d^2}} \leq b \leq \frac{a}{\sqrt{1 + \gamma a^2}}$ $a = \left\{ \frac{40k_o}{\phi_o (R^2 + 1)} \right\}^{1/2} \quad \text{where } R = \frac{d}{a}$ $N = \frac{3\phi_o}{R + 1} \left\{ \frac{\phi_o (R^2 + 1)}{40k_o} \right\}^{1/2}$	$\frac{2r}{ad(1 - \eta r^2)^2}, 0 \leq r \leq \frac{d}{\sqrt{1 + \eta d^2}}$ $h(r) = \frac{2}{a(a-d)} \left(a - \frac{r}{\sqrt{1 - \eta r^2}} \right) (1 - \eta r^2)^{-3/2}$ $\frac{d}{\sqrt{1 + \eta d^2}} \leq r \leq \frac{a}{\sqrt{1 + \eta a^2}}$ $a = \left\{ \frac{20k_o (1 - R^3)}{(1 - R^5) \phi_o} \right\}^{1/2} \quad \text{where } R = \frac{d}{a}$ $N = \frac{3\phi_o^2 (1 - R) (1 - R^5)}{10 (1 - R^3)^2 k_o}$

Table 2. Porosity and permeability variations for the distributions shown in Table 1 assuming the straight capillary model.

DISTRIBUTION	FRACTURE MODEL	TUBE MODEL
Semi-Gaussian	$\phi = \phi_o \frac{a}{\sqrt{\gamma}} \sqrt{\pi} e^{a^2/\gamma} \operatorname{erfc} \sqrt{a^2/\gamma}$ $k = k_o 2\sqrt{2} \left(\frac{a}{\sqrt{\gamma}} \right)^3 e^{a^2/2\gamma} D_{-3} \sqrt{2a^2/\gamma}$ <p>Where D - parabolic cylinder function.</p> $\phi_o = N/a \sqrt{\pi} \quad k_o = N/12 \sqrt{\pi} a^3$	$\phi = \phi_o 2 \frac{a^2}{\eta} \left\{ 1 - a \sqrt{\frac{\pi}{\eta}} e^{a^2/\eta} \operatorname{erfc} (a/\sqrt{\eta}) \right\}$ $k = k_o 4 \frac{a^4}{\eta^2} e^{a^2/2\eta} D_{-4} \sqrt{2a^2/\eta}$ $\phi_o = \pi N / 2a^2$ $k_o = 3N\pi/32 a^4$
Triangular	$\phi = \frac{3\phi_o}{\alpha^2 - \beta^2} \left\{ \sqrt{1+\alpha^2} - \sqrt{1+\beta^2} + \frac{\ln(\alpha + \sqrt{1+\alpha^2})}{\alpha} - \frac{\ln(\beta + \sqrt{1+\beta^2})}{\beta} \right\}$ $k = \frac{10k_o}{\alpha^4 - \beta^4} \left\{ \sqrt{1+\alpha^2} - \sqrt{1+\beta^2} + \frac{3 \ln(\alpha + \sqrt{1+\alpha^2})}{\alpha} - \frac{3 \ln(\beta + \sqrt{1+\beta^2})}{\beta} \right\}$ <p>Where $\alpha = a\sqrt{\gamma}$, and $\beta = d\sqrt{\gamma}$</p> $\phi_o = \frac{N(a+d)}{3} \quad k_o = \frac{N(a^4 - d^4)}{120(a-d)}$	$\phi = \frac{6\phi_o}{\psi^3 - \Omega^3} \left\{ \psi - \Omega + \frac{\ln(1+\psi^2)}{\psi} - \frac{\ln(1+\Omega^2)}{\Omega} + 2 \tan^{-1} \Omega - 2 \tan^{-1} \psi \right\}$ $k = \frac{15k_o}{\psi^5 - \Omega^5} \left\{ \psi - \Omega + \frac{2 \ln(1+\psi^2)}{\psi} - \frac{2 \ln(1+\Omega^2)}{\Omega} + 3 \tan^{-1} \Omega - 3 \tan^{-1} \psi \right\}$ <p>where $\psi = a\sqrt{\eta}$ and $\Omega = d\sqrt{\eta}$</p> $\phi_o = N\pi(a^3 - d^3)/6(a-d) \quad k_o = N\pi(a^5 - d^5)/120(a-d)$
Linear	$\phi = \frac{3\phi_o}{\delta^2} \left\{ \sqrt{1+\delta^2} - 2 + \frac{\ln(\delta + \sqrt{1+\delta^2})}{\delta} \right\}$ $k = \frac{10k_o}{\delta^4} \left\{ \sqrt{1+\delta^2} - 4 + \frac{3 \ln(\delta + \sqrt{1+\delta^2})}{\delta} \right\}$ <p>where $\delta = a\sqrt{\gamma}$</p> $\phi_o = Na/3 \quad k_o = Na^3/120$	$\phi = \frac{6\phi_o}{\lambda^4} \left\{ \lambda^2 - 2\lambda \tan^{-1} \lambda + \ln(1+\lambda^2) \right\}$ $k = \frac{15k_o}{\lambda^6} \left\{ \lambda^2 - 3\lambda \tan^{-1} \lambda + 2 \ln(1+\lambda^2) \right\}$ <p>where $\lambda = a\sqrt{\eta}$</p> $\phi_o = \pi Na^2/6 \quad k_o = \pi Na^4/120$

Table 3. Parameters used in room scale problem.

Parameter	Pillar	Plug	Canister Storage Hole	Storage Tunnel
Permeability (m^2)	10^{-18}	10^{-10}	10^{-10}	10^{-10}
Porosity	0.001	0.50	0.769	0.50
Sp. Heat (J/kg ° C)	953.0	880.0	589.8	840.0
Density ($\frac{kg}{m^3}$)	2780.0	2100.0	2895.0	2780.0
Thermal Cond. ($\frac{J}{m s ° C}$)	2.3	2.192	2.3	50

Table 4. Relative heat-generation rates of waste canisters after emplacement.

Time After Emplacement (yrs.)	Relative Heat-Generation Rate
0	1.0
5	0.849
10	0.723
15	0.621
20	0.539
30	0.424
40	0.361
50	0.330
70	0.285

Table 5. Parameters used in repository-wide model.

Parameter	Saddle Mt.	Wanapum	Grande Ronde
Horiz. Permeability (m^2)	10^{-15}	3×10^{-16}	10^{-16}
Vert. Permeability (m^2)	10^{-17}	3×10^{-18}	10^{-18}
Porosity	0.002	0.001	0.001
Thermal Cond. ($\frac{J}{m \ s \ ^\circ C}$)	2.3	2.3	2.3
Density ($\frac{kg}{m^3}$)	2800.	2800.	2800.
Heat Capacity ($\frac{J}{kg \ ^\circ C}$)	950.	950.	950.

Table 6. Relative changes in formation porosity for different porosity-permeability relationships.

Model	R = 0.669 m		R = 1.5 m		R = 2.784 m	
	42 yrs.	10 yrs.	42 yrs.	10 yrs.	42 yrs.	10 yrs.
Cubic	1.222	1.112	1.038	1.018	1.009	1.004
Series $\phi_c = 0.8$	1.225	1.115	1.039	1.019	1.01	1.004
Series $\phi_c = 0.95$	1.106	1.214	1.019	1.040	1.0045	1.01

Table 7. Extent of boiling and resaturation time with and without inclusion of silica redistribution effects.

	Boiling Volume per canister (m ³)	Radial extent of boiling (m)	Resaturation time (years)
Reference Case	0.46	0.132	44
Series model $\phi_c = 0.95$	≥ 9.2	≥ 0.67	28

Table 8. Vertical flow velocity along the repository axis with and without inclusion of silica redistribution effects.

Case	Vertical Velocity ($\times 10^{-9}$ m/sec) at Times (years)			
	100	500	1000	5000
Reference	0.7170	2.0530	2.3461	2.6093
Series Model $\phi_c = 0.95$	0.7148	2.0537	2.3515	2.6190

This report was done with support from the Department of Energy. Any conclusions or opinions expressed in this report represent solely those of the author(s) and not necessarily those of The Regents of the University of California, the Lawrence Berkeley Laboratory or the Department of Energy.

Reference to a company or product name does not imply approval or recommendation of the product by the University of California or the U.S. Department of Energy to the exclusion of others that may be suitable.

*LAWRENCE BERKELEY LABORATORY
TECHNICAL INFORMATION DEPARTMENT
UNIVERSITY OF CALIFORNIA
BERKELEY, CALIFORNIA 94720*